Study of on-chip cavity magnon polariton devices

by

Sandeep Kaur

A Thesis submitted to the Faculty of Graduate Studies of

THE UNIVERSITY OF MANITOBA

in partial fulfilment of the requirements of the degree of

MASTER OF SCIENCE

Department of Physics and Astronomy

University of Manitoba

Winnipeg.

Abstract

The emerging field of Cavity Spintronics studies the strong coupling of light (photon) with matter (magnons) which leads to the generation of cavity magnon polaritons (CMP). This strong coupling allows energy to be efficiently exchanged between photons and magnons and hence could be used to develop quantum transducers and long-lifetime multimode quantum memories. The CMP systems can be made more suitable for potential practical applications by using planar cavities. Here, a planar tunable cavity was first fabricated that can be used for the on-chip observation of CMP. This planar cavity can also be adapted to be used as a source of pseudo-magnons to achieve pseudo-CMP which could be used to fabricate dynamic filters and to switch devices. In planar CMP systems, a quantitative simulation of the non-resonant radiation damping was also performed by modifying the traditional coupled matrix model to improve our understanding of this coupled system.

Contents

List of Figures

Acknowledgements

First and foremost, I would like to thank my supervisor, Dr. Can-Ming Hu for his constant encouragement and support. His valuable insight and his willingness to guide me towards the right direction to solve problems has helped me a lot to complete this thesis. I would also like to thank Dr. Yongsheng Gui for always being available to answer any questions that I might have and for his continuous help and guidance without which the completion of this thesis and the work therein would have been very difficult.

Furthermore, I would like to acknowledge Dr. John Page and Dr. Gregory Bridges as my thesis examination committee. I would also like to thank the Department of Physics and Astronomy at the University of Manitoba especially Ms. Susan Beshta and Ms. Robyn Beaulieu for their help in ensuring a timely submission of my thesis and for organizing my oral examination. I would like to express my gratitude to the Government of Manitoba for their financial support through the Manitoba Graduate Scholarship.

I would also like to thank Dr. Bimu Yao, and Jinwei Rao for their help in fabricating the microwave resonators that were used for conducting the experiments that have been described in this thesis. Finally, I would like to thank all the members of the Dynamic Spintronics Group for their feedback and useful discussions. I consider myself very fortunate to have had the opportunity to work with such a knowledgeable and helpful group during my graduate program.

Chapter 1

Introduction

The interaction of light with matter gives rise to various physical phenomena such as absorption, spontaneous and stimulated emission as well as the polarizability of the medium which is characterized by its refractive index[1]. The underlying assumption in studying these effects is that the electromagnetic field of the incident light is not strong enough to alter the electronic states of the medium[1]. However, this assumption can easily breakdown if the incident electromagnetic field or the interaction is strong. In this case, the mixing between the electrodynamics of the incident light and the material dynamics leads to the generation of a quasi-particle that has both photon-like and material-like properties and is known as a 'polariton'[2]. For a homogeneous medium, the electric permittivity, ϵ, and the magnetic permeability, μ, can be assumed to be frequency and wave vector independent. However, due to material dynamics, it is possible that an excitation is generated that has a dipole moment due to which the electric permittivity or the magnetic permeability have a frequency or wave vector dependence as well as a resonance[3]. In this case, the electric and magnetic fields of the propagating light can strongly couple with the resonant material dynamics and generate polaritons[3].

The polariton was first discovered independently by both Tolpygo[4] and Huang[5] who were theoretically studying the coupling between electromagnetic fields and the vibrations in a crystal lattice (phonons) that leads to the generation of phonon-polaritons. Since there are many different

material dynamics that can lead to the generation of an electric or magnetic dipole moment which can couple to the electromagnetic field of the incident radiation, there are many different types of polaritons that are generated and have been studied[3]. For example, the coupling between visible light and exciton (a quasi-particle resulting from the coupling between an electron-hole pair) leads to the generation of exciton polariton[6], whereas, the strong coupling between cavity photons and excitons leads to the generation of cavity exciton polaritons[7, 8]. In both the cases, the coupling between the electron-hole pair generates an electric dipole moment that couples with the electromagnetic field of the visible light. The electromagnetic field of the incident radiation can also couple with the magnetic dipole moment generated due to magnons (quasi-particle formed due to the collective excitation of electron spins) in a magnetic crystal. This coupling leads to the generation of magnon-polaritons[3].

Following the discovery of polariton, this area of research evolved greatly over the years during which different types of polaritons were theoretically and experimentally studied. This not only led to a better understanding of the basic physics of how light interacts with matter in different scenarios but also led to the creation of new areas of research such as cavity exciton polaritons[9] and cavity magnon polaritons (CMP)[10]. The strong coupling of cavity photons and magnons was first theoretically studied by Soykal and Flatte[11] who predicted that this coupling could be achieved at microwave frequencies by using a nano-magnet. Following this theoretical realization, continuous research in this area has led to the development of various potential practical applications[12].

However, the previously used experimental CMP systems have some limitations in terms of adaptation for practical applications. This is because they often consist of a 3-D cavity and require an electromagnet to tune the resonance frequency of the magnon mode. Therefore, to use the CMP systems for potential practical applications, it is important to develop on-chip planar tunable CMP systems that do not rely on an electromagnet. Furthermore, characterizing the radiation damping in such planar CMP systems through experiments and quantitative simulations would also be useful for the design and adaptation of these systems for practical applications.

1.1 General Model of Polariton Dispersion using Maxwell's Equations

Even though the different polaritons that have been briefly described above have different material dynamics from which they originate, it is possible to have a general theoretical approach that describes the frequency dispersion of the incident light due to the generation of polaritons. Firstly, the propagation of the incident electromagnetic radiation in matter can be described by using the Maxwell's equations in SI units as

$$\begin{aligned} \nabla \times \mathbf{E} &= -\frac{\partial \mathbf{B}}{\partial t}, \\ \nabla \times \mathbf{H} &= \frac{\partial \mathbf{D}}{\partial t}, \end{aligned} \tag{1.1}$$

where $\mathbf{E}, \mathbf{D}, \mathbf{B}, \mathbf{H}$ are the electric field, electric displacement field, magnetic field, and magnetic field strength, respectively. The electric displacement field and the magnetic field strength are related to the electric field and the magnetic field, respectively according to the relations

$$\begin{aligned} \mathbf{D} &= \epsilon_0 \epsilon(\mathbf{k}, \omega)\mathbf{E}, \\ \mathbf{B} &= \mu_0 \mu(\mathbf{k}, \omega)\mathbf{H}, \end{aligned} \tag{1.2}$$

where ϵ_0, μ_0 are the electric permittivity and magnetic permeability of the free space, respectively; whereas $\epsilon(\mathbf{k}, \omega), \mu(\mathbf{k}, \omega)$ are the frequency (ω) and wave vector ($\mathbf{k}$) dependent electric permittivity and magnetic permeability, respectively generated due to a dipole carrying excitation in a medium.

Using the relations given in Eq. (1.2), the two Maxwell's equations given by Eq. (1.1) can be combined to obtain a single equation that contains only the electric field as

$$c^2(\nabla \times (\nabla \times \mathbf{E})) + \epsilon(\mathbf{k}, \omega)\mu(\mathbf{k}, \omega)\frac{\partial^2 \mathbf{E}}{\partial t^2} = 0, \tag{1.3}$$

where c is the speed of light in vacuum. A similar equation can be obtained which contains the magnetic field only. As described in Ref. [3], when the frequency dependent permittivity and permeability are isotropic, the solutions of the above equation that are of interest are the ones for which the electric field **E** is perpendicular to the wave vector **k**. Assuming that the electric field has a form similar to the plane wave i.e. $E \propto e^{i(\mathbf{k}x-\omega t)}$), the dispersion relation for the transverse wave that satisfies the above equation is given by

$$\omega^2 = \frac{c^2|\mathbf{k}|^2}{\epsilon(\mathbf{k},\omega)\mu(\mathbf{k},\omega)}. \tag{1.4}$$

When the permittivity and permeability are both independent of the frequency and the wave vector, the above equation gives

$$\omega = \frac{c|\mathbf{k}|}{\sqrt{\epsilon\mu}}, \tag{1.5}$$

which is the well-known linear dispersion relation of frequency with the wave vector **k**. Therefore, in the case where the ϵ and μ are both independent of the frequency and the wave vector, the light simply travels through the medium with a velocity that is different than the velocity of light in vacuum by a factor of $1/\sqrt{\epsilon\mu}$. However, when ϵ or μ is frequency and wave vector dependent, the frequency dispersion due to the generation of polaritons can be calculated using Eq. (1.4) by substituting the appropriate form of $\epsilon(\mathbf{k},\omega)$ ($\mu(\mathbf{k},\omega)$) for polaritons formed due to the coupling between the electric (magnetic) field of the incident light with the electric (magnetic) dipole moment generated due to material dynamics[3].

1.2 Calculating Frequency Dispersion due to Phonon-Polaritons

In order to see how Eq. (1.4) can be used to calculate the polariton frequency dispersion consider a simple case of phonon-polaritons. In diatomic crystals, the lattice vibrations give rise to long wavelength optical phonons which can produce an electric dipole moment in each unit cell[3, 5]. This leads to the generation of transverse optical phonons which can strongly couple with the transverse incident electromagnetic waves to produce the phonon-polaritons.

To study the frequency dispersion due to the generation of these phonon-polaritons the electric permittivity and magnetic permeability are assumed to be isotropic in order have a solution of the form of Eq. (1.4). Therefore, in this case, the magnetic permeability of the crystal is assumed to be 1 and the electric permittivity is considered to be isotropic in the limit the wave vector **k** is very small[3]. Hence, it can be assumed that the electric permittivity essentially depends only on the frequency and is independent of the wave vector. The total permittivity of the crystal, in the absence of any damping, can therefore be written as

$$\epsilon(\omega) = \epsilon_0 + \frac{\Omega_p^2}{\omega_T^2 - \omega^2}, \tag{1.6}$$

where ϵ_0 is the electric permittivity from all other sources of polarization except from the motion of the lattice, ω_T is the resonance frequency of the transverse phonons in the crystal, and $\Omega_p^2 = \dfrac{4\pi n e'^2}{m}$ is the effective unscreened plasma frequency for the lattice which has n unit cells per unit volume with reduced mass m. e' is the effective charge of ions in a unit cell of the lattice. A detailed derivation of this equation from the relative motion of sublattices can be found in Ref. [3].

Equation (1.6) exhibits a resonant structure that allows the electrical permittivity of the medium to affect the propagation of light with frequency near the transverse phonon mode frequency ω_T. Thus, the frequency dispersion of light can be obtained by substituting the expression for the

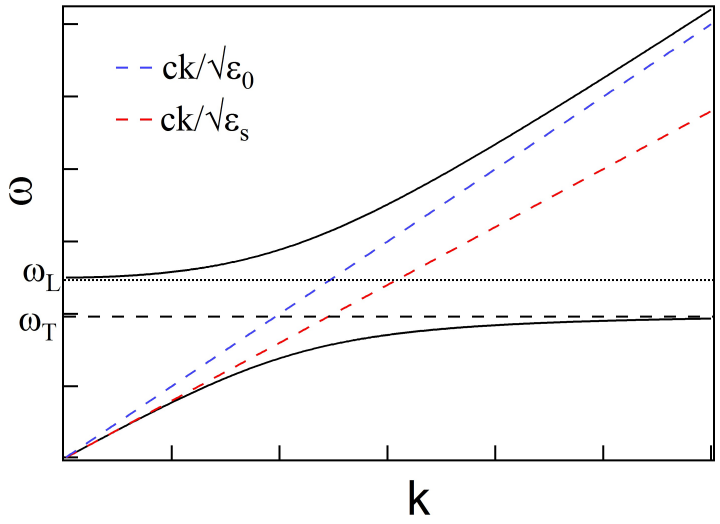

Figure 1.1: Frequency dispersion plotted as a function of the wave vector shows the presence of the two polariton branches that undergo anti-crossing. The black, blue, and red dashed lines show the uncoupled frequency dispersion of the transverse phonon mode, the incident light in vacuum, and in medium, respectively; the dotted line represents the longitudinal phonon mode[3, 5].

permittivity shown above into Eq. (1.4) as

$$\omega^2 = \frac{c^2|\mathbf{k}|^2}{\epsilon_0 + \dfrac{\Omega_p^2}{\omega_T^2 - \omega^2}}, \tag{1.7}$$

from which the frequency can be solved for in terms of the wave vector as being

$$\omega_\pm^2 = \frac{\dfrac{c^2|\mathbf{k}|^2}{\epsilon_0} + \omega_T^2 + \Omega_p^2 \pm \sqrt{(\dfrac{c^2|\mathbf{k}|^2}{\epsilon_0} - \omega_T^2 - \Omega_p^2)^2 + \dfrac{4c^2|\mathbf{k}|^2\Omega_p^2}{\epsilon_0}}}{2}. \tag{1.8}$$

The result from the above equation has been plotted in Fig. 1.1 which shows the presence of two frequencies for each value of wave vector **k** which correspond to the two branches of the polariton modes generated due to the interaction between the transverse phonon modes and the transverse incident electromagnetic field.

As shown in Fig. 1.1, as $|\mathbf{k}| \to 0$, the resonance frequency for the lower polariton branch

goes to 0; whereas, the resonance frequency of the upper polariton branch approaches ω_L which corresponds to the resonance frequency of the long-wavelength longitudinal phonon modes[3, 5]. At this frequency, $\epsilon(\omega) = 0$ because for a longitudinal wave, the electric field $\mathbf{E}$ is always parallel to the wave vector $\mathbf{k}$ and the electric displacement field $\nabla \cdot \mathbf{D} = \epsilon(\omega)\nabla \cdot \mathbf{E}$ can only be 0 when $\epsilon(\omega) = 0$. Here, $\nabla \cdot \mathbf{D} = 0$ because there are no free charges present in a crystal[3]. The resonance frequency of the longitudinal phonon modes can be calculated by setting $\epsilon(\omega) = 0$ in Eq. (1.6) which gives

$$\omega_L^2 = \omega_T^2 + \frac{\Omega_p^2}{\epsilon_0}. \tag{1.9}$$

which can also be written as $\frac{\omega_L}{\omega_T} = \sqrt{\frac{\epsilon_s}{\epsilon_0}}$ where $\epsilon_s = \epsilon_0 + \frac{\Omega_p^2}{\omega_T^2}$ is the static or the zero frequency electrical permittivity[3]. The longitudinal phonon modes do not couple with the transverse incident electromagnetic field due to which their resonance frequency remains unchanged[5] as shown by the dotted line in Fig. 1.1. When $|\mathbf{k}| \to \infty$, the frequency of the lower polariton branch approaches ω_T, whereas the frequency of the upper polariton branch approaches the limiting behaviour of $\omega = \frac{c|\mathbf{k}|}{\sqrt{\epsilon_0}}$ as shown by the blue dashed line in Fig. 1.1. This implies that the frequency of the incident light is much higher than the frequency of the light that can excite the oscillation of crystal lattice and couple with it to generate phonon-polaritons. Therefore, when $\mathbf{k} \to \infty$ the incident light will simply pass through the crystal.

Figure 1.1 clearly shows the anti-crossing between the two polariton branches that are separated by a forbidden frequency (or Rabi) gap of $\omega_L - \omega_T$ where $\epsilon(\omega)$ is negative[3]. This generation of two hybridized modes or polariton branches whose resonance frequency dispersion shows an anti-crossing behaviour is a general feature which has been used to study the various different types of polaritons[1, 3].

1.3 Emergence of Cavity Polaritons

Following the theoretical description of polaritons by Huang[5], this concept was readily adapted to describe the interaction of electromagnetic waves with the different material dynamics such as excitons and magnons[12]. The field of polariton research regained momentum when cavity exciton polaritons were demonstrated experimentally due to the strong coupling of excitons with cavity photons[9, 12]. In this case, the solutions to the Maxwell's equations must satisfy additional boundary conditions being imposed due to the cavity due to which only certain wave vectors can exist. To study cavity exciton polaritons, planar optical Fabry-Perot cavities that are made of two highly reflecting mirrors are used[1]. The resulting cavity exciton polaritons are highly non-linear and have a non-parabolic dispersion along with a very small effective mass. Therefore, these polaritons allow the observation of Bose-Einstein condensation, super-fluidity and spatial coherence over a long range[1, 12].

Continuous research in this area has led to the development of various practical applications such as electrically pumped low threshold polariton lasers, all optical logic circuits that include polariton diodes and quantum polaritonics which are polariton-based quantum electronics[1, 12]. The cavity exciton polaritons could also be used as quantum bits (qubits) for the development of quantum memories due to their ability to undergo Rabi oscillations between cavity photon and exciton states[1]. Such cavity photon-exciton coupling based quantum memories could be used to speed up computations and have potential applications in quantum simulation and quantum cryptography[1].

In general, the coupling regime where polaritons are formed is known as the strong coupling regime. This regime occurs when the energy dissipation rates due to electrodynamics of incident light and the material dynamics is much smaller than the coupling strength between the systems[1, 11, 12]. In a cavity photon-exciton system the dissipation losses occur due to the reflectivity of the mirrors as well as due to the energy lost by the excitons. This coupling can be described by using

the Hamiltonian for the coupled system under the rotating wave approximation[1] as

$$H = \begin{bmatrix} E_p - i\gamma_p & \Omega_R/2 \\ \Omega_R/2 & E_e - i\gamma_e \end{bmatrix} \tag{1.10}$$

where E_p, E_e are the dispersion relations of the energies of the cavity photons and excitons, respectively. γ_p, γ_e are the dissipation losses of the cavity photons and excitons, respectively with a coupling strength Ω_R which is known as the Rabi energy[1]. The real part of the eigenvalues of the above matrix can be used to calculate the frequency/energy dispersion as a function of the energy detuning ($E_p - E_e$). This plot would reveal an anti-crossing feature between the upper and lower polariton branches. The imaginary part of the eigenvalues reveals the evolution of the dissipation losses of the two systems. Therefore, this Hamiltonian model provides an alternative pathway to calculate the resonance frequency dispersion of the system due to the generation of cavity exciton polaritons and can be easily extended to describe other polariton systems. A more detailed description about the derivation of this Hamiltonian can be found in Ref. [1].

While the cavity photon-exciton coupling experiments are performed at optical frequencies by using semiconductor materials[1, 12], in 2010, it was theoretically predicted that strong cavity photon-magnon coupling could be achieved at microwave frequencies by using a nano-magnet[11]. In 2013, Huebl et al.[13] provided the first experimental demonstration of this strong cavity photon-magnon coupling at a cryogenic temperature of 50 mK by using the magnons in an yttrium iron garnate (YIG) sample and microwave photons from a superconducting coplanar waveguide. Since the cavity photon-magnon coupling strength is proportional to the square root of number of spins present in the magnon sample ($\sqrt{N}$)[13, 14, 15], YIG is often chosen as a source of magnons to achieve stronger coupling strengths due to its higher spin density compared to paramagnetic spin ensembles[13, 14]. Furthermore, YIG also has low damping[13, 14] due to which it can be used observe the strong cavity photon-magnon coupling regime which requires that the cavity photon-magnon damping rates should be much smaller than the coupling strength between them. The initial interest in this research area was to achieve quantum strong cavity photon-magnon coupling

for the purpose of achieving efficient transfer of quantum information between the cavity photon and magnon states via Rabi oscillations[12]. Therefore, in order to achieve such quantum coupling cryogenic conditions were required due to which the initial experimental work was performed at low temperatures[13, 14].

However, in 2014, it was demonstrated by Zhang et al.[15], that this strong cavity photon-magnon coupling and classical Rabi-like oscillations could also be observed at room temperatures. They further showed that by tuning their cavity, they could classically observe the different coupling regimes (Strong, Weak, Magnetically induced transparency and Purcell) that were defined by the ratios between the cavity photon-magnon coupling strength to the cavity and magnon dissipation rates[15]. In 2015, Bai et al.[10] showed that this coupling leads to the generation of CMP which can be electrically detected and described by using a classical electrodynamics model. This model describes the cavity photon-magnon coupling by using the Ampère's and Faraday's Laws and hence, differs from the earlier studies which mostly used the quantum Hamiltonian to describe this coupling. A more detailed description of these two models will be given in the next chapter.

The pioneering work in this field described above has brought forward an important question regarding the difference between the quantum and classical regimes of the cavity photon-magnon coupling[12]. Since, the strong cavity photon-magnon coupling can be achieved both at cryogenic as well as room temperatures and the commonly studied experimental features (resonance frequency anti-crossing and linewidth exchange) can be described by using the quantum theory[13, 15] or by using the Maxwell's equations for macroscopic electromagnetic fields[10] it becomes difficult to distinguish between the quantum and classical regimes of the CMP system. Therefore, new experiments are being designed to probe the boundary between the quantum and classical regimes and to search for experimental features that can be exclusively described by quantum mechanics[12].

Furthermore, continuous research work in this area has also led to the development of various potential practical applications for the CMP systems such as the development of quantum transducers that have the ability to coherently link various quantum systems[16], long-lifetime multi-mode

quantum memories wherein the Rabi oscillations between the cavity photon and magnon states could be used as a quantum bit[12, 16] and quantum repeaters[17]. However, the experimental systems that are often used to study the cavity photon-magnon coupling consist of a 3-D cavity and almost exclusively rely on an electromagnet to tune the resonance frequency of the YIG magnon modes to observe the CMP. These requirements make the CMP system not very suitable for potential practical applications. Therefore, it is important to develop an on-chip CMP system that does not rely on an electromagnet. Moreover, it is important to completely characterize the sources of damping in planar CMP systems for the design and adaptation of these systems for potential practical applications.

1.4 Thesis Outline

The research objectives for this thesis were to make the cavity photon-magnon coupled system more suitable for potential practical applications and to modify the theoretical model to better understand the cavity photon-magnon coupling physics and describe the various experimental results that were obtained. This thesis is divided into 4 chapters. The first chapter, as seen here discusses the history of polariton research and gives an overview of the field of CMPs by summarizing some of the pioneering research work in this area and discussing an important unsolved problem regarding the design and adaptation of these systems for practical applications. In the second chapter, the different theoretical models: classical harmonic oscillator, quantum Hamiltonian, and the classical electrodynamics model have been described. The features of a common matrix model that arises from these different theoretical models has also been discussed there. In the third chapter, some important background information required to experimentally study the cavity photon-magnon coupled system has been first described. This is then followed by a discussion of the experiments that were performed to meet the research objectives described above. The final chapter of this thesis summarizes the results of these experiments and outlines some of the future research work that could be performed.

Chapter 2

Theory

In order to understand and explain the cavity photon-magnon coupling, in this chapter, a brief review of the different theoretical models that have been proposed is presented. In general, this coupling can be described by using the coupled harmonic oscillator analogy which assumes that the cavity mode and the magnon mode can be modelled as two harmonic oscillators that are coupled to each other via a coupling constant κ. From this harmonic oscillator picture, the resonance frequency dispersion that shows the generation of polaritons and the linewidth evolution of the cavity photon and the magnon mode can be calculated by using either the quantum hamiltonian or the classical equations of motion for the coupled harmonic oscillator system. Each of these two methods is presented in detail in the following sections of this chapter. Furthermore, another method proposed by Bai et. al.[10] that uses classical electrodynamics to study the cavity photon-magnon coupling is described. This classical electrodynamics model describes the origin of the cavity photon-magnon coupling from the phase correlation effect arising from Faraday's and Ampère's laws. Yet, the final equation, that can be used to theoretically model the cavity photon-magnon coupling, obtained from these three different methods remains the same and is a 2 x 2 matrix. In the final section, it is shown how this two coupled oscillator system described by a 2 x 2 matrix can be expanded to an N-coupled oscillator system to describe the coupling between multiple cavity and/or magnon modes.

2.1 Classical Harmonic Oscillator Model

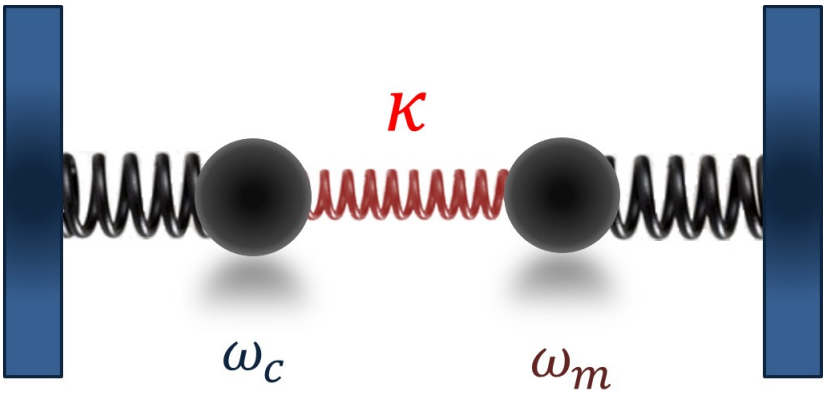

Figure 2.1: Schematic diagram of the two coupled harmonic oscillator model that can be used to describe the cavity-photon magnon coupling.

As described previously, the cavity photon magnon coupling can be represented by using a coupled harmonic oscillator system as shown in Fig. 2.1. In this figure the two oscillators have a unit mass, a resonance frequency of ω_c and ω_m and represent the microwave cavity photon and the magnon modes, respectively. These two oscillators are coupled via a coupling constant κ. Let β and α be the damping of the oscillators representing the cavity and the magnon mode, respectively. These damping constants are used to model the intrinsic losses of the cavity and the Gilbert damping of the magnon mode. A detailed description of the effect of Gilbert damping on the magnon mode is given in the next chapter. The derivation of equations of motion for this system [Eq. (A.10)] has been discussed in detail in Appendix A.

The derived equations of motion can be written in a 2 x 2 matrix format as

$$\begin{bmatrix} \omega^2 - \omega_c^2 + i\omega\omega_c\beta & -\kappa\omega_c^2 \\ -\kappa\omega_c^2 & \omega^2 - \omega_m^2 + i\omega\omega_c\alpha \end{bmatrix} \begin{bmatrix} A_c \\ A_m \end{bmatrix} = \begin{bmatrix} -f \\ 0 \end{bmatrix}. \tag{2.1}$$

Here, f is the driving force acting on the oscillator representing the cavity photon mode, the diagonal terms represent the resonance of the harmonic oscillators that model the cavity mode and the

magnon mode, respectively and the off-diagonal terms denote the coupling between them. From this matrix equation, it can be easily seen that in the absence of the coupling term (i.e. $\kappa = 0$), only the resonance of the cavity mode oscillator will be observed i.e. $A_m = 0$. By solving for ω from the determinant of the above matrix [given by Eq. (A.12)], two roots are obtained. The real part of the roots gives the resonance frequency dispersion for the two oscillators; whereas, the imaginary part of the roots gives the linewidth evolution of the two modes[18]. These two results can therefore be used to explain the experimentally obtained data in CMP experiments which shows the generation of the 'Rabi gap of the CMP'[19] and the linewidth evolution of the cavity photon and the magnon mode.

When $\omega_c = \omega_m$ i.e. the resonance frequency of the two oscillators is matched, the real part of the eigenfrequencies of this system [Eq. A.13] can be simplified such that

$$\omega_{\pm} = \omega_c \pm \frac{\kappa\omega_c}{2}. \tag{2.2}$$

Thus, the resonance frequency difference between the two hybridised modes is given by $\Delta\omega_{gap} = \omega_+ - \omega_- = \kappa\omega_c$. Therefore, if the cavity resonance frequency is known, the coupling strength between the two resonators can be determined experimentally from the 'Rabi gap of CMP'.

The theoretical model briefly described here is sufficient to model the frequency dispersion and the linewidth exchange between the two resonators. However, in order to relate the amplitudes of oscillation (A_c, A_m) of the oscillators to the microwave transmission that is usually measured in experiments, Harder et. al[18] developed a formalism that can be used to calculate the input and output energy of the system. This is achieved by connecting an absorber, which models the measurement system, to the cavity mode oscillator. If it is assumed that the output oscillator has no damping, then the output energy and hence the microwave transmission is found to be proportional to $|A_c|^2$ where

$$|A_c|^2 = \frac{|\omega^2 - \omega_m^2 + i\alpha\omega\omega_c|^2}{|det(\Omega)|^2}. \tag{2.3}$$

and $det(\Omega)$ is the determinant of the coupling matrix given by Eq. (A.12). An exact quantitative

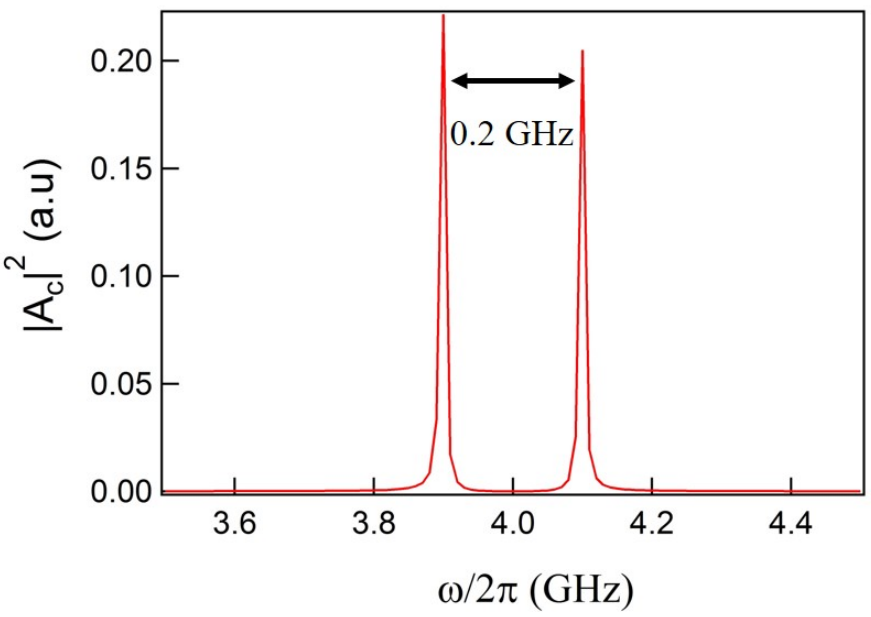

Figure 2.2: Simulated amplitude of oscillation, obtained from the classical harmonic oscillator model Eq. (2.3), shows the generation of two hybridized modes with $\Delta\omega_{gap}/2\pi = 0.2$ GHz.

relationship between the microwave transmission and $|A_c|^2$ along with its detailed derivation can be found in Ref. [18]. Figure 2.2 shows a simulated oscillation amplitude ($|A_c|^2$) curve plotted as a function of frequency at $\omega_c/2\pi = \omega_m/2\pi = 4$ GHz which is similar to the experimentally obtained microwave transmission curve obtained in cavity photon-magnon coupling experiments. Here, $\alpha = 0.0002$ and $\beta = 0.003$. This figure clearly shows the generation of two hybridized modes, separated by a frequency difference of $\Delta\omega_{gap}/2\pi = 0.2$ GHz which is dependent on the coupling strength $\kappa = 0.05$ between the oscillators.

When $\omega_c \neq \omega_m$, there will be less efficient transfer of energy between the two modes due to which the peak amplitudes of the two modes will be different. Using the real and imaginary parts of the roots of Eq. (A.12), the resonance frequency and the linewidth of the two modes can be simulated and have been plotted as a function of the detuning $\Delta = \omega_m - \omega_c$ in Figs. 2.3(a) and (b), respectively. These figures show the two key features that are often used to experimentally study the cavity photon-magnon coupling[10, 12, 15, 18]. Figure 2.3(a) shows that the coupling between the two modes leads to generation of the Rabi gap due to the generation of CMP; whereas, Fig.

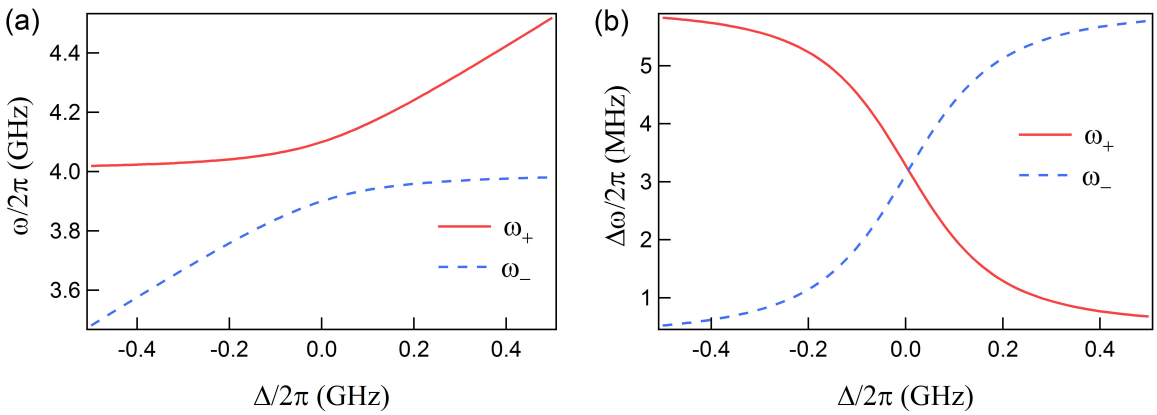

Figure 2.3: Simulated (a) resonance frequency and (b) linewidth of the cavity photon-magnon modes obtained from the classical harmonic oscillator model Eq. (A.12) plotted as a function of the detuning Δ

2.3(b) shows the linewidth evolution of the two modes.

Therefore, by using the classical harmonic oscillator model, the microwave transmission line-shape, resonance frequency dispersion as well as the linewidth of the hybridized cavity photon-magnon modes can be described. The advantages of using this model is that it is relatively easy to use and it directly demonstrates the harmonic nature of the cavity photon-magnon coupling. This model can also be easily extended to describe the coupling between multiple oscillators[18]. This possibility of extending the harmonic oscillator model [Eq. (2.1)] will be discussed in more detail in the final section of this chapter.

2.2 Quantum Hamiltonian Model

While the previous model provided a macroscopic classical description of the cavity photon-magnon coupling, this coupling can also be explained by using a microscopic quantum theory of spins and electromagnetic fields[18]. The Hamiltonian for the interaction between the cavity photons and the spins of a ferri/ferromagnetic material can be written as $H = H_{spin} + H_{photon} + H_{coupling}$ where H_{spin}, H_{photon}, and $H_{coupling}$ are the Hamiltonians that describe the spin, photon, and the interaction between these two systems, respectively.

While the actual form of this Hamiltonian might be very complex, some assumptions/approximations can be made to simplify it. One such approximation is the rotating wave approximation in which all the rapidly oscillating terms of the Hamiltonian can be neglected[15]. Along with this approximation if it is assumed that there exists only one cavity mode and one magnon mode, then the Hamiltonian of this system can be written as

$$\begin{aligned} H/\hbar - \frac{\omega_c + \omega_m}{2} &= \omega_m m^\dagger m + \omega_c p^\dagger p + \kappa_q (p^\dagger m + m^\dagger p) \\ &= \begin{bmatrix} p^\dagger & m^\dagger \end{bmatrix} \begin{bmatrix} \omega_c & \kappa_q \\ \kappa_q & \omega_m \end{bmatrix} \begin{bmatrix} p \\ m \end{bmatrix}. \end{aligned} \tag{2.4}$$

Here, ω_m, ω_c are the resonance frequencies of the magnon and the cavity mode, respectively, $p^\dagger$, (p) is the photon creation (annihilation) operator, $m^\dagger$ (m) is the magnon creation (annihilation) operator, and κ_q is the coupling strength between the cavity and the spin system[15, 16, 18]. This is the Dicke model or the N spin version of the Jaynes Cummings model, known as the Tavis Cummings model[13, 18]. This model gives the quantum description of two coupled harmonic oscillators in which one oscillator corresponds to the spin system and the other corresponds to the electromagnetic field of the cavity. The coupling strength κ_q in this case is related to microscopic parameters, and is given by

$$\kappa_q = \frac{\eta\gamma}{2}\sqrt{\frac{\hbar\omega_c\mu_0}{V}}\sqrt{2Ns}, \tag{2.5}$$

where, V is the volume of the cavity, γ is the gyromagnetic ratio, N is the total number of spins in the ferri/ferromagnetic sample, s is the spin number for a ground state ion of the sample, and η is the overlap factor[15, 20].

The overlap factor determines the energy exchange efficiency between the cavity mode and the spin system and can be written as

$$\eta = |\frac{\int(\mathbf{h}_{rf} \cdot \mathbf{m})dV_s}{h_{max}m_{max}V_s}|, \tag{2.6}$$

where, h_{max} is the maximum magnetic field due to the cavity, $\mathbf{h}_{rf}$ is the amplitude of the microwave magnetic field at a distance r where the magnetic sample is located, V_s is the volume of the magnetic sample, **m** is the time dependent off z-axis magnetization[20]. Therefore, the overlap factor and hence the coupling strength between the cavity photon-magnon system depends on the relative location of the spin system inside the cavity. Furthermore, Eq. (2.5) shows that the coupling strength is proportional to the square root of the number of spins present in the system. Therefore, in order to experimentally achieve strong photon-magnon coupling, a magnetic sample with a high spin density is desirable as mentioned in the previous chapter. The eigenvalues of the Hamiltonian given in Eq. (2.4) can then be written as

$$\omega_{\pm} = \frac{\omega_c + \omega_m \pm \sqrt{(\omega_c - \omega_m)^2 + 4\kappa_q^2}}{2}. \tag{2.7}$$

Here again, when $\omega_c = \omega_m, \omega_{gap} = \omega_+ - \omega_- = 2\kappa_q$[13, 18]. The microwave transmission through the cavity photon-magnon system can also be calculated using this quantum theory along with the Green's function for a photon; a detailed derivation for this can be found in Ref. [18].

Hence, the quantum theory of spins and electromagnetic fields can be simplified to obtain the quantum coupled harmonic oscillator model which can be used to describe the cavity photon-magnon coupling. The advantage of using this model is that it shows the coupling strength dependence on the number of spins (N) in the magnetic sample and on the overlap factor (η) which was otherwise not predicted by the classical harmonic oscillator model described previously.

2.3 Classical Electrodynamics Model

The previously described classical harmonic oscillator model does not outline the physical origin of the cavity photon-magnon coupling. To overcome this limitation, Bai et. al[10] proposed a classical dynamic phase correlation model in which they attribute the origin of the CMP to electrodynamic coupling arising from Faraday's and Ampère's Laws. Figure 2.4 shows a schematic diagram that can be used to explain the classical electrodynamics model. As shown in this figure, in the absence of coupling, the cavity resonance can be modelled by using an LCR circuit which has an inductor with inductance L, a capacitor with capacitance C and a resistor with resistance R connected in series. This circuit carries a microwave current $j_x + ij_y$. The cavity resonance frequency is therefore given by $\omega_c = \dfrac{1}{\sqrt{LC}}$ and the damping, normalized with respect to the cavity resonance frequency is given by $\beta = R\sqrt{\dfrac{C}{L}}$.

Without coupling, the dynamic magnetization precession of the ferri/ferromagnetic sample is solely governed by the Landau-Lifshitz-Gilbert (LLG) equation. A more detailed description of how the LLG equation can be used to solve for the magnetization precession and ferromagnetic resonance has been given in the next chapter. Nonetheless, the solution for the magnetization precession using the LLG equation can be written as $m = Am_x + im_y = me^{-i\omega t}$[10, 18] where $A = \omega_0/\omega_m$, $\omega_0 = \gamma H$ and ω_m is the resonance frequency of the magnetization precession which depends on the geometry of the sample. For example, for a spherical sample, $\omega_m = \gamma(H + H_a)$ with an applied magnetic field H along the z-direction. Here, H_a is the anisotropy field which depends on the geometry, and is usually much smaller than H; therefore, $A \simeq 1$.

When this ferri/ferromagnetic sample is placed inside a microwave cavity, the magnetization precession induces an additional voltage due to Faraday's Law. This induced voltage can be written as

$$\begin{aligned} V_x &= K_c L \frac{dm_y}{dt}, \\ V_y &= -K_c L \frac{dm_x}{dt}, \end{aligned} \tag{2.8}$$

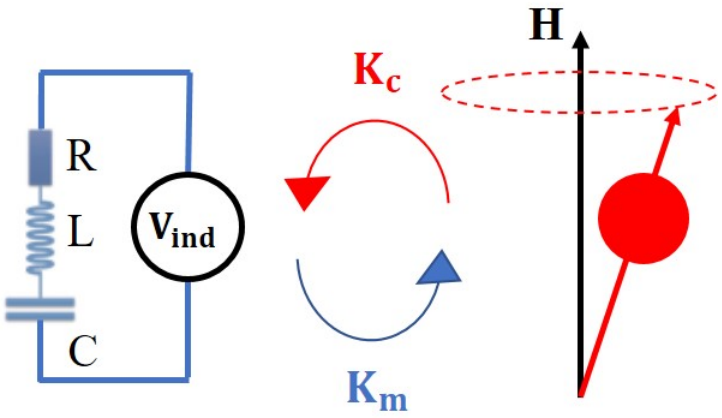

Figure 2.4: Schematic diagram of the classical electrodynamics model proposed by Bai et. al[10] that describes the coupling between a cavity mode represented as an LCR circuit and the magnetization precession of a ferri/ferromagnetic spin system.

where, K_c is the coupling constant that determines the phase relation between the cavity photon and magnon due to Faraday's Law. The total induced voltage $V_{ind} = V_x + iV_y = -K_c L\omega m$ can be added to the cavity LCR circuit as an additional voltage source which in turn changes the microwave current in the cavity as $V_{ind} = jZ_c$. Here, Z_c is the impedance of the LCR circuit that is used to model the cavity and is given by $Z_c = \frac{-iL}{\omega}(\omega^2 - \omega_c^2 + i\beta\omega\omega_c)$. The additional microwave current, generated due to the induced voltage, would then affect the microwave field that drives the magnetization precession[10]. According to Ampère's Law, the relationship between the microwave field generated due to the microwave current can be written as

$$\begin{aligned} h_x &= K_m j_y, \\ h_y &= -K_m j_x, \end{aligned} \tag{2.9}$$

where, K_m is the coupling constant that determines the phase relation between the cavity photon and magnon due to Ampère's Law.

From the LLG equation, the magnetization can now be written as $m = \frac{i\omega_0 K_m j}{\omega - \omega_m + i\alpha\omega}$ where α is the Gilbert damping associated with the magnon mode, and $\omega_0 = \gamma M_0$ with M_0 being the saturation magnetization. Therefore, the equations of motion that describe the electrodynamic

cavity photon-magnon coupling due to both Faraday's and Ampère's Laws can be written as

$$\begin{aligned} \frac{-iL}{\omega}(\omega^2 - \omega_c^2 + i\beta\omega\omega_c)j &= -K_c L\omega m, \\ i\omega_0 K_m j &= (\omega - \omega_m + i\alpha\omega)m, \end{aligned} \tag{2.10}$$

or in matrix format as

$$\begin{bmatrix} \omega^2 - \omega_c^2 + i\beta\omega\omega_c & i\omega^2 K_c \\ -i\omega_0 K_m & \omega - \omega_m + i\alpha\omega \end{bmatrix} \begin{bmatrix} j \\ m \end{bmatrix} = \begin{bmatrix} 0 \\ 0 \end{bmatrix}. \tag{2.11}$$

The determinant of this 2 x 2 matrix is given by $(\omega^2-\omega_c^2+i\beta\omega\omega_c)(\omega-\omega_m+i\alpha\omega)-\omega^2\omega_0 K_c K_m$. Similar to the classical harmonic oscillator model that was described previously, the resonance frequency dispersion and the linewidth evolution of the cavity photon-magnon modes can be found by using the real and imaginary parts of the roots of this determinant[10]. Here, the coupling strength K between the cavity photon and the magnon mode is given by $K = \sqrt{K_c K_m}$. If $\alpha, \beta \ll 1$, the roots can be easily calculated as being

$$\omega_\pm = \frac{\omega_c + \omega_m \pm \sqrt{(\omega_c - \omega_m)^2 + K^2\omega_0\omega_c}}{2}. \tag{2.12}$$

If $\omega_c = \omega_m, \omega_{gap} = \omega_+ - \omega_- = K\sqrt{\omega_0\omega_c}$[10, 18]. Therefore, the electrodynamic coupling strength can be directly estimated from the experimental data by using the frequency separation between the two hybridized modes generated. The microwave transmission can also be calculated using this classical electrodynamic model by using the microwave circuit theory and a detailed derivation has been presented in Ref. [18].

Therefore, the classical electrodynamics model is valuable since it can both explain the origin as well as the key features of the cavity photon-magnon coupling by using the phase correlation due to Ampère's and Faraday's Laws. This model can also be easily extended to describe the coupling between multiple cavity photon and magnon modes[10, 18].

2.4 Features of the Matrix Model

In the previous sections, three different models have been described that can be used to model the cavity photon-magnon coupling. While each of these three models have their own origin and advantages, these models give a similar 2 x 2 coupling matrix whose general form can be written from Eqs. (2.1, 2.4, and 2.11) as being

$$\Omega = \begin{bmatrix} \text{Cavity resonance} & \text{Coupling term} \\ \text{Coupling term} & \text{Magnon resonance} \end{bmatrix}. \tag{2.13}$$

In this matrix, the diagonal elements contain the terms that describe the uncoupled resonance of the cavity mode and the magnon mode; whereas, the off-diagonal elements represent the coupling between the cavity and the magnon modes. Such a 2 x 2 matrix is obtained irrespective of which theoretical model is chosen to describe the cavity photon-magnon coupling. The real and imaginary parts of the eigenvalues of this matrix can then be used to model the resonance frequency dispersion and the linewidth evolution of the cavity photon and magnon modes which are the two key experimental features that have been used to experimentally study the cavity photon-magnon coupling[15, 10, 18].

Using the above described general form of the coupling matrix (Ω), this matrix model can be easily extended to describe a cavity photon-magnon coupling system that has multiple cavity and/or magnon modes. For example, consider a system that contains 2 magnon modes separately coupled with a single cavity mode. This system can then be described by a 3 x 3 matrix given by

$$\Omega = \begin{bmatrix} \text{Cavity resonance} & \kappa_1 & \kappa_2 \\ \kappa_1 & \text{Magnon1 resonance} & \kappa_3 \\ \kappa_2 & \kappa_3 & \text{Magnon2 resonance} \end{bmatrix}, \tag{2.14}$$

where, κ_1 (κ_2) is the coupling term between the cavity mode and the magnon mode 1 (2), and κ_3 is the coupling between the two magnon modes. Here again, the diagonal elements are the

resonance terms describing the cavity and the 2 magnon modes; whereas, each pair of the off-diagonal elements describe the coupling between the cavity mode and the respective magnon mode.

The coupling terms in the above matrices are different for each of the three different models that have been described in the previous sections. For experimental results obtained for a macrospin system at room temperature, either of those three models can be used to describe the cavity photon magnon coupling i.e. no difference will be observed for the results obtained from the quantum or the two classical models[12]. However, some differences may arise at low temperatures or in a few spin system wherein the quantum nature of this coupling may become dominant due to the breakdown of the assumptions that allow the simplification of the quantum Hamiltonian model to a quantum coupled harmonic oscillator system. Therefore, the cavity photon-magnon coupling could be used to explore the boundary between the quantum and classical regimes[12].

The relationship between κ, κ_q and K (the coupling strengths for the classical harmonic oscillator, the quantum Hamiltonian and the classical electrodynamics model) can be determined for the case when $\omega_c = \omega_m$ from Eqs. (A.13, 2.7, and 2.12) as

$$\Delta\omega_{gap} = \kappa\omega_c = 2\kappa_q = K\sqrt{\omega_0\omega_c}, \tag{2.15}$$

where, $\kappa_q = \dfrac{\eta\gamma}{2}\sqrt{\dfrac{\hbar\omega_c\mu_0}{V}}\sqrt{2Ns}$[15]. Therefore, in the harmonic oscillator limit, the coupling strengths obtained from the classical harmonic oscillator and the phase correlation models can also be related to microscopic parameters.

In this thesis, the classical harmonic oscillator model is extended and modified to describe the various experimental results that were obtained. These results have been presented in detail in the next chapter.

Chapter 3

Experiment and Results

In this chapter, the main experimental results related to the topic of cavity photon-magnon coupling are presented. Firstly, a short background section is provided which describes the knowledge that forms the basis for experimentally studying this cavity photon-magnon coupling. Then the following three sections of this chapter describe in detail the three main results that were obtained i.e. voltage control of cavity photon-magnon coupling, non-resonant radiation damping in CMP systems and voltage tunable pseudo cavity photon-magnon coupling.

3.1 Background

As described in the previous chapter, the cavity photon-magnon coupling studies the interaction or the energy exchange efficiency between a cavity photon and a ferri/ferromagnetic spin system. The cavity photon-magnon coupling is often experimentally studied in the microwave (GHz) regime because efficient THz radiation generation and detection electronics are still under development. Traditionally, the external magnetic field is required to tune the resonance frequency of the spin system. In this work, alternative ways to study the cavity photon-magnon coupling are explored which do not require the external magnetic field and may make this system more suitable for potential practical applications. These alternative methods can be devised by using an artificially engineered structure known as a split ring resonator (SRR) that has an effective magnetic

permeability and can either enhance/oppose the incident electromagnetic radiation based on its relative orientation[21, 22]. Thus, a SRR could either be used to design a cavity or be used a source of pseudo magnons in the cavity photon-magnon coupling experiments to replace the ferromagnetic sample. Both of these alternatives have been explored in detail in the following sections of this chapter. But firstly, in this section a detailed discussion of the elements required for studying the cavity photon-magnon coupling and the reasoning used for the selection of particular components in carrying out the experiments is presented.

3.1.1 S-Parameter Measurement

In this thesis, the cavity photon-magnon coupling is experimentally studied by measuring the microwave transmission through this system. The microwave propagation through any system can be described by using the transmission line theory. This theory has the ability to describe wave propagation in terms of voltage, current and impedance[23]. Therefore, it has been widely used at radio and microwave frequencies to describe wave propagation through cavities, transmission lines and resonators etc by modelling them as lumped capacitances, and inductances. It is also being extensively employed to describe the response of metamaterials operating in GHz range[24, 25]. A key feature of the transmission line theory is that it provides us the ability to analyse microwave networks that are just a cascade connection of two port networks by simply using the Transmission (ABCD) matrix. For a two-port network shown in Fig. 3.1(a), the transmission matrix is defined as

$$\begin{bmatrix} V_1 \\ I_1 \end{bmatrix} = \begin{bmatrix} A & B \\ C & D \end{bmatrix} \begin{bmatrix} V_2 \\ I_2 \end{bmatrix}, \tag{3.1}$$

where V_1, I_1 are the input voltage and current applied at Port 1; whereas, V_2, I_2 are the output voltage and current at Port 2. The advantage of using the transmission matrix is that for a cascade connection of two port networks, the overall transmission matrix can be found by simply multiplying the transmission matrix for each individual network.

However the drawback of using the ABCD matrix is that it is difficult to measure the input

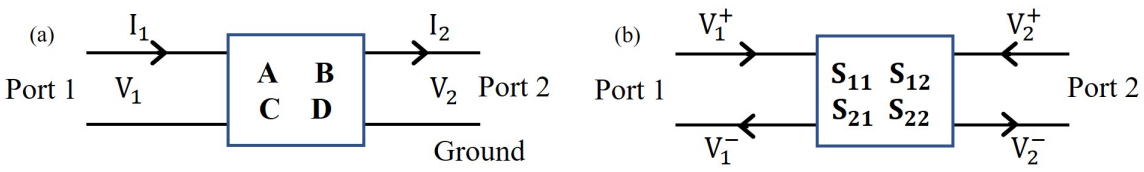

Figure 3.1: (a) The transfer and (b) the scattering matrix parameters for a two-port network.

or transmitted microwave current and voltage due to which the microwave transmission is experimentally measured in terms of the scattering (S) parameters[23]. The S-parameters of an active or passive microwave network are the ratios of the voltage waves reflected from, to the voltage waves incident on any microwave port i[23]. In general, the S-parameters measure the microwave reflection and transmission through a system. In microwave range, the magnitude and phase of these parameters are usually measured by a vector network analyzer(VNA) which consists of two or four channels. For a two port network shown in Fig. 3.1(b), the scattering or the S-matrix is given by

$$[S] = \begin{bmatrix} S_{11} & S_{12} \\ S_{21} & S_{22} \end{bmatrix}, \tag{3.2}$$

where $S_{ij} = \dfrac{V_i^-}{V_j^+} \mid_{V_i^+=0}$ with V_i^- being the voltage wave that is reflected from port i when a voltage wave V_j^+ is made incident on port j[23]. Therefore, the general naming convention used to define the S-parameters is $S_{[outputport][inputport]}$. Hence, for a two-port network S_{11}, or S_{22} measures the microwave signal reflected from the system when the microwaves are input at port 1 or port 2, respectively. Whereas, S_{12} and S_{21} measure the microwave signal transmitted through the system when the microwaves are input at port 2 and port 1, respectively. For a reciprocal system (which is often the case for a cavity photon-magnon coupled system) $S_{12} = S_{21}$. The S-parameters can be easily obtained from the ABCD parameters by applying the conversion equation

$$\begin{bmatrix} S_{11} & S_{12} \\ S_{21} & S_{22} \end{bmatrix} = \begin{bmatrix} \dfrac{A+\dfrac{B}{Z_0}-CZ_0-D}{A+\dfrac{B}{Z_0}+CZ_0+D} & \dfrac{2(AD-BC)}{A+\dfrac{B}{Z_0}+CZ_0+D} \\ \dfrac{2}{A+\dfrac{B}{Z_0}+CZ_0+D} & \dfrac{-A+\dfrac{B}{Z_0}-CZ_0+D}{A+\dfrac{B}{Z_0}+CZ_0+D} \end{bmatrix}, \tag{3.3}$$

where $Z_0 = 50\Omega$ is the characteristic impedance of the input and output ports which is a design standard chosen for optimal power handling and signal loss per unit length[23]. Therefore any microwave network can be analysed by using the transmission (ABCD) matrix formalism described above and then converted in terms of the S-parameters that can be experimentally measured by using a VNA.

The advantages of using a VNA for the S-parameter measurement is that a VNA can make very accurate measurements by taking into account a variety of possible errors by using an in-built error correction model and a calibration process[23]. For the experiments described in the following sections, the microwave transmission (S_{21}) was measured by using a calibrated two-port Agilent PNA 5230C VNA.

3.1.2 Ferromagnetic Resonance

The cavity photon-magnon coupling physics essentially studies the interaction between cavity photons and the spins of a ferri/ferromagnetic material in the presence of an externally applied magnetic field. Here, a magnon is a quasiparticle that is generated due to the collective excitation of electron spins in a magnetic material. The effect of magnetic fields on the spins of a ferromagnetic material was first studied by Lev Landau and Evgeny Lifshitz in 1935[26]. They described that if a magnetic field (**H**) is applied in a direction perpendicular to the magnetization (**M**) of a ferromagnetic material, the external field will exert a torque on the magnetization which will cause it to precess along the direction of **H** as shown in Fig. 3.2(a). This torque is given by

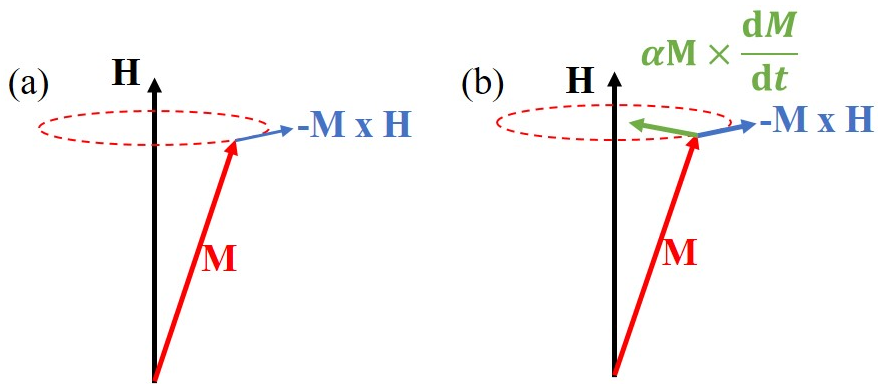

Figure 3.2: Sketch of the magnetization precession around an applied magnetic field (a) without damping and (b) with Gilbert damping.

$$\frac{d\mathbf{M}}{dt} = -\gamma \mathbf{M} \times \mathbf{H}, \tag{3.4}$$

where γ is the electron gyromagnetic ratio in the material. This equation was modified by T. L. Gilbert to include the effects of magnetic damping within the material[27]. The modified equation referred to as the Landau-Lifshitz-Gilbert (LLG) equation is given as

$$\frac{d\mathbf{M}}{dt} = -\gamma \mathbf{M} \times \mathbf{H} + \frac{\alpha \mathbf{M}}{M_0} \times \frac{d\mathbf{M}}{dt}, \tag{3.5}$$

where α is the Gilbert damping factor which describes how quickly the precession of the moments will stop and M_0 is the component of the magnetization that lies along the direction of the external field. A schematic representation of this system is shown in Fig. 3.2(b). If the effect of internal demagnetization field is taken into account then the effective magnetic field acting on the system can be written as $\mathbf{H}_{eff} = \mathbf{H} - \mathbf{N} \cdot \mathbf{M}$ where $\mathbf{N}$ is the demagnetization factor whose value is different along different directions. The demagnetization field exists due the preference of the magnetic moments to align along the easy axis which would correspond to a smaller value of N in that direction.

The LLG equation describes that without the presence of a continuous driving torque, the amplitude of magnetization precession will decrease due to damping and the magnetization will

eventually align along the direction of the effective applied magnetic field. To maintain the magnetization precession, a continuous driving torque is required which can be obtained by using a microwave magnetic field ($\mathbf{h}e^{-i\omega t}$) which oscillates with a frequency ω. The magnitude of this field is usually much smaller than the magnitude of the externally applied magnetic field. In this case, the magnetization $\mathbf{M}$ can be written as $\mathbf{M} = M_0\widehat{\mathbf{k}} + \mathbf{m}e^{-i\omega t}$, where $\mathbf{m}e^{-i\omega t}$ is the oscillating component of the magnetization due to the microwave magnetic field and is much smaller than M_0. The solution from the LLG equation can then be written as $\mathbf{m} = \chi\mathbf{h}^{in}$ or

$$\mathbf{m} = \begin{bmatrix} \chi_{xx} & i\chi_{xy} & 0 \\ -i\chi_{yx} & \chi_{yy} & 0 \\ 0 & 0 & 0 \end{bmatrix} \begin{bmatrix} h_x^{in} \\ h_y^{in} \\ h_z^{in} \end{bmatrix}, \tag{3.6}$$

where $h_x^{in}, h_y^{in}, h_z^{in}$ are the components of the microwave magnetic field inside the sample and χ is the Polder tensor which describes the motion of the magnetization due to an oscillating magnetic field. The components of this tensor are given by

$$\begin{aligned} \chi_{xx} = \chi_{yy} &= \frac{(\omega_0 - i\alpha\omega)\omega_m}{\omega_0^2 - \omega^2 - 2i\alpha\omega\omega_0}, \\ \chi_{xy} = \chi_{yx} &= \frac{\omega\omega_m}{\omega_0^2 - \omega^2 - 2i\alpha\omega\omega_0}, \end{aligned} \tag{3.7}$$

where $\omega_m = \gamma M_0$, $\omega_0 = \gamma H$ is the resonance frequency of the magnetization precession and the Gilbert damping is assumed to be much smaller than 1 [28]. This resonance of the magnetization precession is referred to as the ferromagnetic resonance (FMR).

For the experimental observation of strong cavity photon-magnon coupling, a ferri/ferromagnetic sample that has a small Gilbert damping factor and high spin density is desirable. These requirements can be met by using a spherical yttrium iron garnet (YIG, $Y_3Fe_5O_{12}$) sample. The crystal structure of YIG is shown in Fig. 3.3. This figure shows that the oxygen (O^{2-}) ions form three types of polyhedrons namely the dodecahedron, the octahedron and the tetrahedron[29]. The yttrium (Y^{3+}) ion occupies the dodecahedral site whereas the iron (Fe^{3+}) ions occupy the tetrahedral

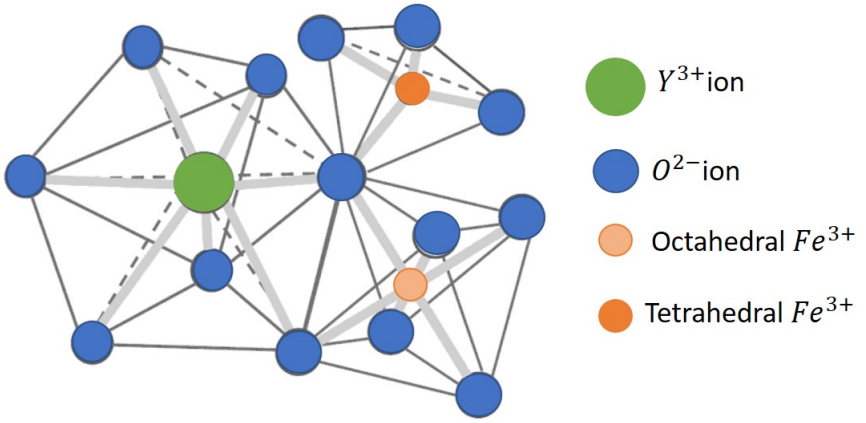

Figure 3.3: Schematic diagram of the crystal structure of YIG as described in Ref. [29]

and octahedral sites. The Fe^{3+} ions which are in these two different sites have a difference in spin which results in the magnetic behaviour of this compound[29]. YIG spheres have a high quality factor due to which they have been used for designing tunable microwave filters and resonators[30]. YIG has a very low Gilbert damping factor $\sim 10^{-5}$ and a very high spin density of $\sim 10^{27}m^{-3}$ due to which it is often used for cavity photon-magnon coupling experiments[15, 31, 32]. Thus, in the experiments that have been described in the following sections a 1 mm diameter YIG sphere was chosen to be used as a source of magnons.

3.1.3 Magnetic Response of Split Ring Resonator

The pseudo spin system or cavity used in this thesis is a SRR. The design of a SRR was first proposed by Pendry et. al.[21] and is shown in Fig. 3.4(a). It consists of two concentric split-rings made up of non-magnetic materials at a distance 'd' from each other. Even though these rings have their own response, a composite structure of these rings is used in order to ensure that incident electromagnetic radiation interacts with them as a homogeneous medium. This composite structure exhibits an effective magnetic permeability (μ_{eff}) in the presence of microwave radiation given by the equation

$$\mu_{eff} = 1 - \frac{F\omega^2}{\omega^2 - \omega_0^2 + i\omega\alpha_s\omega_0}, \tag{3.8}$$

where $F = \frac{\pi r^2}{a^2}$, r is the radius of the inner ring, a is the size of the unit cell of the composite medium, ω_0 is the resonance frequency of the SRR given by $\omega_0 = \sqrt{\frac{3l}{\pi^2\mu_0 C r^3}}$ and α_s is the damping of the SRR given by $\alpha_s = \frac{2l\rho}{r\mu_0\omega_0}$[21]. Here l is the spacing between the layers of rings, C is the capacitance due to the gap between the rings and ρ is the resistance per unit length of the rings that is measured around the circumference. While the loops of the SRR can be concentric circles or squares as needed, the splits in the SRR ensure that the resonant wavelength is much larger than the diameter of the rings. In this design, the orientation of the two rings is such that the two splits are opposite to each other so that the direction of the currents induced in the two rings is opposite to each other. This generates a capacitive interaction between the two rings which significantly lowers the resonance frequency of the structure as compared to the resonance frequency of a single SRR[22].

In 2000, Smith et al.[22] adapted this design in order to experimentally demonstrate that a composite array of SRRs not only has a magnetic permeability but this permeability could be negative at high frequencies. The negative permeability was discovered from the presence of a gap in the frequency dispersion curve. Since, it was assumed that the permittivity of this structure is always positive, it was inferred that the gap in the frequency dispersion curve was due to the presence of a region with negative permeability. It was also shown that by adding wires between the split rings, as shown in Fig. 3.4(b), a negative refractive index could be achieved[22, 34]. Therefore, these artificially engineered structures could exhibit properties that are difficult or impossible to find in nature. Such materials are referred to as metamaterials and they were first theoretically described in 1968 by V. G. Veselago[35]. Following the experimental demonstration by Smith et al.[22], various different types of metastructures have been proposed that can be used for a variety of different potential applications such as in designing super lenses, electromagnetic cloaks etc[36].

SRRs are one of the most commonly used metamaterials due to their compact size and high

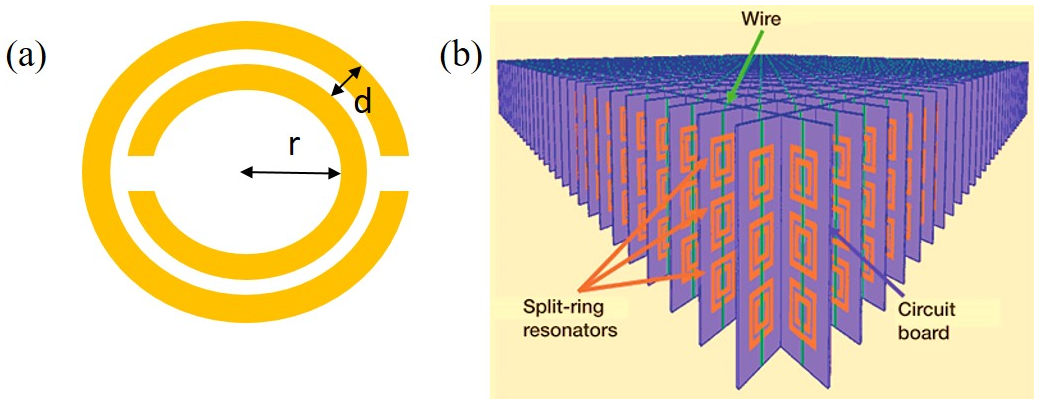

Figure 3.4: (a)Schematic diagram of the SRR proposed by Pendry et. al.[21] and fabricated by Smith et. al.[22]. (b) Schematic diagram of a composite array of square SRRs with wires at the back[33]. This array can be used to achieve a negative refractive index[34].

sensitivity. Due to these characterisitics, SRRs have been successfully adapted to be used as bio-sensors and to detect the dielectric properties of various liquids[37, 38]. This is because of the fact that the SRRs can be oriented in such a way that they are excited by both the electric and the magnetic field of the incident electromagnetic radiation[21, 22]. This induces a strong current in the SRR which allows it to either enhance/oppose the incident electromagnetic field. Therefore, SRRs have the potential to being used as a cavity to perform photon-magnon coupling experiments. Furthermore, due to the effective magnetic response of the SRR, it has the potential of being used as a pseudo magnon source to replace the YIG sample in these experiments. In the cavity photon-magnon coupling experiments described below, a SRR has been used either as a cavity or as a source of pseudo-magnons in order to achieve additional tunability of this coupling from which further potential practical applications of this system are proposed.

3.2 Voltage Control of Cavity Photon-Magnon Coupling

As described in the previous chapter, the cavity photon-magnon coupling, which leads to the generation of CMP, is being extensively investigated and has many potential practical applications[13, 14, 15, 10, 16, 17, 18, 31, 32, 39]. It has been demonstrated that this coupling offers a promising approach to develop long-lifetime broadband, multi-mode quantum memories[16], quantum repeaters[16] and quantum transducers that could coherently link different quantum systems together [17]. However, the experimental systems that have been previously used to demonstrate the cavity photon-magnon coupling have limitations in terms of adapting them for practical applications. This is because they often consist of a 3-D cavity and an YIG sample and employ an electromagnet to tune the coupling strength between the cavity photons and the YIG magnons by changing the resonance frequency of the magnons. The previous experimental systems exclusively rely on an electromagnet to tune the cavity photon-magnon coupling because the cavities that have been used have a fixed resonance frequency. Therefore, the development of a planar tunable cavity whose resonance frequency can be easily and continuously tuned would eliminate the requirement of an electromagnet to study the cavity photon-magnon coupling. Such a cavity would also help in easier integration of this photon-magnon coupling system to on-chip devices for advanced spintronic applications[13, 39].

3.2.1 Design and Characterization of the Planar Tunable Cavity

In order to develop a planar cavity that satisfies all the above mentioned requirements, DC voltage controlled metamaterials can be used. These materials have been used in the past to develop switch-able metamaterial absorbers[40] or zero index arrays[41]. Thus, this technique can be adapted to achieve a planar metamaterial cavity whose resonance frequency can be controlled by using a DC voltage.

To achieve this goal, a rectangular SRR with a tapered transmission line was chosen to function as a planar cavity as shown in Fig. 3.5. A rectangular instead of the usual circular SRR design was

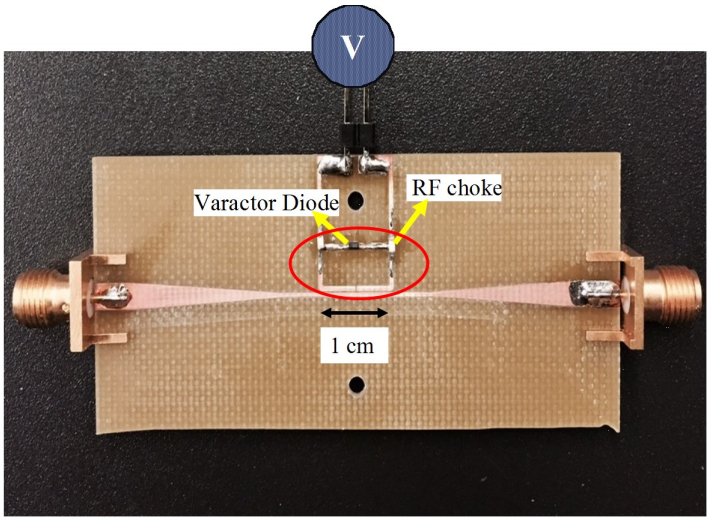

Figure 3.5: Photograph of the fabricated varactor loaded SRR cavity.

chosen in order to maximize the coupling between the transmission line and the resonator. The SRR had a length and a width of 10 mm and 5 mm, respectively with a slit-width of 0.2 mm. The SRR was fabricated on a printed circuit board (PCB) that had a 1.5 mm thick FR-4 substrate using the LPKF Protomat machine. The width of the copper strip used for fabrication was 0.2 mm. The tapered transmission line had a length of 7 cm and its thickness varied from 3 mm at the edges to 0.2 mm at the center. The microwave current was sent via the transmission line which in turn excited the SRR's resonance through inductive coupling. A Skyworks SMV-2019 varactor diode was integrated along an edge of the SRR as shown in Fig. 3.5 and two inductors (RF chokes) were soldered on either side of the SRR to decouple the microwave circuit from the DC-voltage bias circuit. The capacitance of the varactor diode changes from 2.22 pF to 0.3 pF as the applied DC voltage changes from 0 to 20 V[42]. This in turn changes the capacitance as well as the resonance frequency of the SRR.

The resonance frequency of the SRR cavity can be measured by connecting it to a VNA. The measured microwave transmission $|S_{21}|$ through the varactor loaded SRR cavity at different DC voltage biases is shown in Fig. 3.6(a). Due to the non-linear response of the varactor diode, the $|S_{21}|$ line shape is not pure Lorentzian at low applied voltages as can be seen in Fig. 3.6(a). Nevertheless, the resonance frequency of this cavity can be easily and continuously tuned from

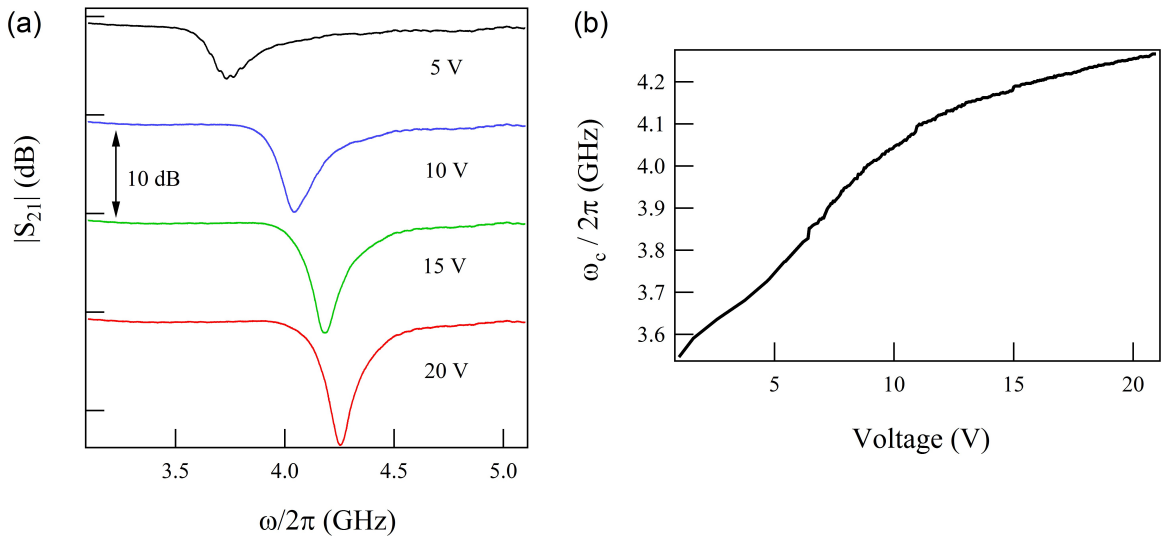

Figure 3.6: (a) (Offset for clarity) Plot of the experimentally measured transmission spectra for the SRR at different applied voltages. (b) Resonance frequency of the SRR cavity as a function of the applied voltage.

3.55 GHz to 4.27 GHz by changing the applied voltage as shown in Fig.3.6(b).

3.2.2 YIG Sample Characterization

In order to demonstrate the voltage control of the CMP using the varactor loaded SRR cavity, the dispersion of the uncoupled magnon modes of the YIG sample should be first measured. For this, a tapered transmission line with the same parameters as the one used to excite the SRR was fabricated (length = 7 cm, width varying from 3 mm at edges to 0.2 mm at the center) on a 1.5 mm thick FR-4 substrate PCB board. A 1 mm diameter spherical YIG sample was placed just above the center of this transmission line which was then placed between the poles of an electromagnet. The microwave transmission through this system was then measured by connecting the transmission line to a VNA as shown by the schematic diagram in Fig. 3.7.

The magnetic field produced by the electromagnet (along the z-axis) is perpendicular to the microwave magnetic field (in the x-y plane) generated by the current flowing in the transmission line. The microwave magnetic field also has a spatial variation over the diameter of the YIG sample.

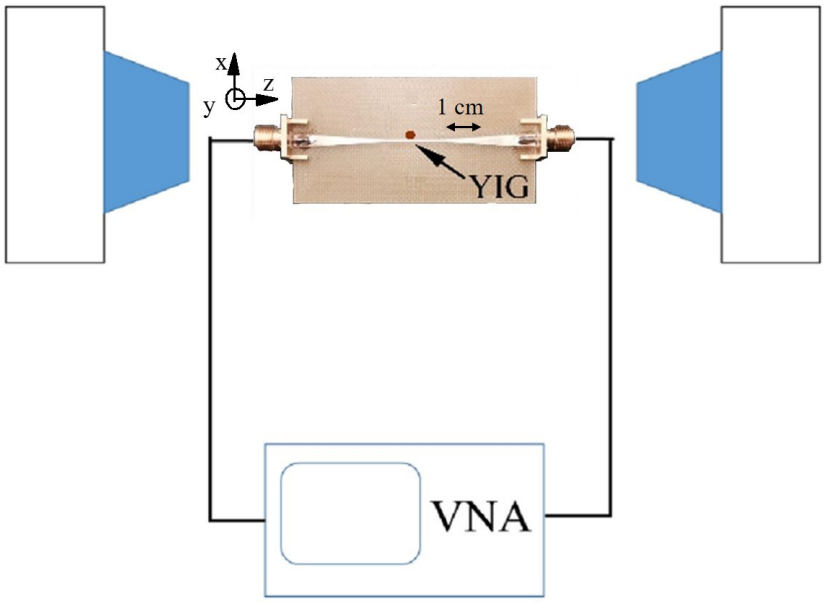

Figure 3.7: Schematic diagram of the measurement setup used to measure the dispersion of the YIG magnon modes.

Due to this spatial variation of the driving microwave magnetic field, higher order magnetostatic modes (long wavelength spin waves) of the YIG sample are excited[43] as shown by the plot of transmission amplitude in the top panel of Fig. 3.8 which was measured at 157.4 mT. Here, the amplitudes of the first and the fourth modes have been multiplied by a factor of 5 so that they can be clearly seen. These magnetostatic modes can be labelled by using the (n,m,k) classification scheme proposed by Walker[44]. According to this scheme, index n and m refer to the r-f magnetization reversal sectors in the z-direction and in the x-y plane, respectively[44]. The index k is used to label the mode which has more than one solution[20] and for simplicity it is assumed that k = 0 which corresponds to the lowest order mode. The dominant mode in the transmission amplitude spectra corresponds to the (1,1,0) mode. The other higher order modes visible in Fig. 3.8 are believed to be the (3,1,0), (2,2,0) and (4,1,0) modes. By continuously tuning the applied magnetic field, several transmission spectra can be measured and have been plotted as a mapping in the bottom panel of Fig. 3.8. This figure clearly shows the frequency dispersion of the different magnetostatic modes along with their relative amplitudes as a function of the applied magnetic

field.

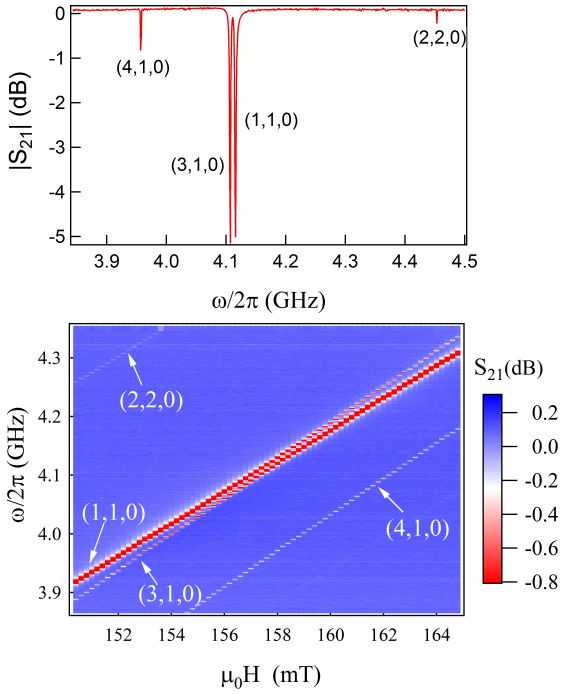

Figure 3.8: Transmission amplitude spectra at 157.4 mT and the transmission amplitude mapping for the YIG sample measured using a tapered transmission line shows the different magnetostatic modes.

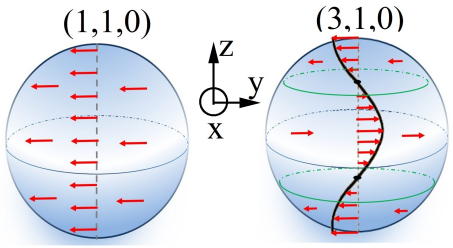

Figure 3.9: The r-f magnetization for the (1,1,0) and (3,1,0) modes

The r-f magnetization for the (1,1,0) and the (3,1,0) mode has been plotted in Fig. 3.9. The (1,1,0) mode corresponds to the uniform magnetostatic mode where the r-f magnetization always points in the same direction. However, the (3,1,0) mode has 3 sectors of r-f magnetization reversal along the z-direction as shown by Fig. 3.9. These two magnetostatic modes can couple with each other due to the effect of dipole-dipole and exchange interactions on the dispersion of these

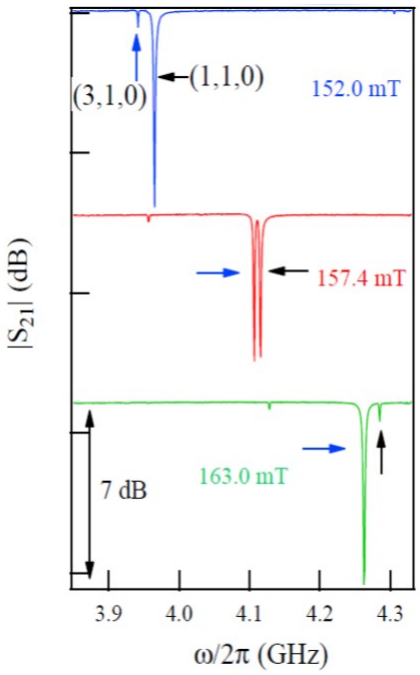

Figure 3.10: (Offset for clarity) Plot of the measured transmission spectra as a function of frequency shows the coupling between the two magnetostatic modes of YIG

modes[43, 45] as shown by the plot of transmission spectra in Fig. 3.10. The black and the blue arrows in this figure are used to indicate the high and low frequency modes, respectively. This figure shows that the two magnetostatic modes [(1,1,0) and (3,1,0)] couple to produce two hybridized modes at 157.4 mT.

The resonance position and linewidth of these two coupled modes can be obtained by fitting the transmission spectra using a combination of symmetric and anti-symmetric Lorentz lineshapes[46] given by the equation

$$|S_{21}| = \frac{A_1\Delta\omega_1^2 + B_1\Delta\omega_1(\omega-\omega_{01})}{(\omega-\omega_{01})^2+\Delta\omega_1^2} + C_1 + \frac{A_2\Delta\omega_2^2 + B_2\Delta\omega_2(\omega-\omega_{02})}{(\omega-\omega_{02})^2+\Delta\omega_2^2} + C_2. \tag{3.9}$$

Here, $\Delta\omega_1, \Delta\omega_2$ are the linewidths of the two modes, ω_{01}, ω_{02} are the resonance frequencies of the modes, C_1, C_2 are the offsets, A_1, A_2, and B_1, B_2 are the scaling factors for the symmetric and anti-symmetric Lorentzian lineshapes for the two modes.

The resonance frequencies and linewidths, obtained from fitting the transmission spectra using

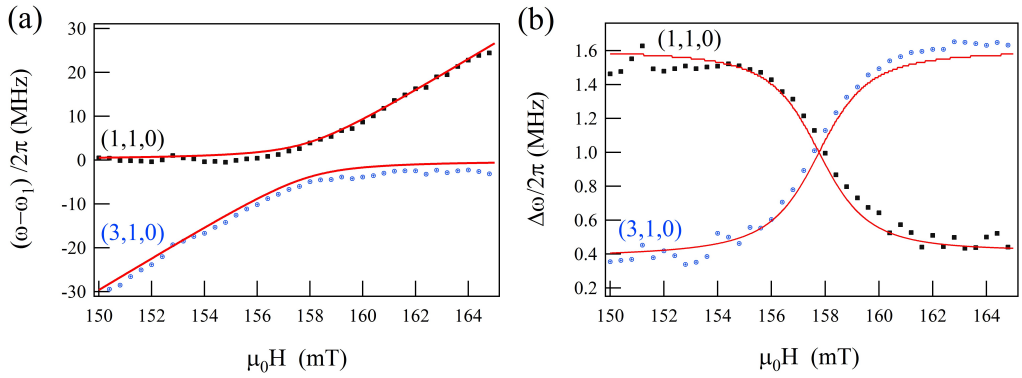

Figure 3.11: Experimentally (symbol) and analytically (solid line) obtained (a) resonance position and (b) linewidth of the coupled magnetostatic modes plotted as a function of the applied magnetic field

the above equation, have been plotted as a function of the applied magnetic field in Fig.3.11(a) and (b), respectively. Here, the resonance position of the modes is obtained by subtracting the linear dispersion of the (1,1,0) mode given by $\omega = \gamma(H + H_0)$ in the simplest approximation, where $\gamma = 171.4\mu_0$GHz/T is the gyromagnetic ratio and $\mu_0 H_0 = -6.76$ mT is the field related to the orientation of the sphere with respect to the applied magnetic field[47, 48]. The anti-crossing feature associated with coupling can thus be clearly seen from Fig. 3.11(a), whereas the linewidth evolution of the two modes can be seen in Fig. 3.11(b). This magnetostatic mode coupling can be modelled in a classical picture using the two coupled harmonic oscillator model as described previously in the Theory chapter. For this model, the damping parameters α and α_2 for the (1,1,0) and (3,1,0) modes can be estimated to be 0.0009 and 0.0002, respectively from the linewidth of the modes obtained by fitting the transmission spectra using Eq. (3.9) when the modes are uncoupled. Since α, $\alpha_2 \ll 1$, the coupling strength g = 0.0019 has been calculated from the frequency gap $\Delta\omega_{gap} \simeq g\omega'$ where ω' is the resonance frequency at which the two hybridized modes have equal amplitude. The resonance frequency and linewidth evolution can then obtained by solving for the real and imaginary parts of the determinant of the coupling matrix given by Eq. (A.12). The result has been plotted as solid lines in Fig. 3.11(a) and (b), respectively where good agreement between the experimental and the analytical results can be seen.

3.2.3 Magnetic Control of the Cavity Photon-Magnon Coupling

After characterizing the magnetostatic modes of the YIG sample, the coupling between the YIG magnon modes and the photons of the tunable SRR cavity can be studied. To do so, the YIG sphere was placed along the width of the SRR (i.e. on one of the vertical arms) where the microwave current and hence the microwave magnetic field is maximum. The system was connected to a VNA and placed between the poles of an electromagnet such that the magnetic field produced by the electromagnet was perpendicular to the driving microwave magnetic field. The DC voltage applied to the cavity was set at 11 V which corresponds to a resonance frequency of 4.08 GHz. Figure 3.12 shows a series of the measured S_{21} spectra plotted as a function of the microwave frequency at different applied magnetic fields where the red, green and blue arrows are used to identify the modes with the highest, intermediate and lowest resonance frequency. The modes can only be clearly labelled far from the coupling region because in the coupling regime only hybridized modes exist. Figure 3.12 shows that the (1,1,0) mode strongly couples with the cavity mode at 160.0 mT to produce the CMP; whereas the (3,1,0) mode does not couple with the cavity mode and simply passes through it. The difference in the respective mode magnetizations of the (1,1,0) and (3,1,0) mode[49] may be responsible for the difference in their coupling strength with the cavity mode since the coupling strength between the cavity mode and the magnon mode is dependent on the overlap factor (η) which is in turn dependent on the mode magnetization [shown by Eq. (2.6)] [20]. Instead of coupling to the cavity mode, the (3,1,0) mode is magnetically coupled to the two branches of the CMP produced by the cavity photon-magnon coupling between the cavity mode and the (1,1,0) mode.

By fitting the measured transmission spectra using a combination of the symmetric and anti-symmetric Lorentzian lineshapes [an extension of Eq. (3.9) to $|S_{21}| = \frac{A_1\Delta\omega_1^2 + B_1\Delta\omega_1(\omega-\omega_{01})}{(\omega-\omega_{01})^2+\Delta\omega_1^2} + C_1 + \frac{A_2\Delta\omega_2^2 + B_2\Delta\omega_2(\omega-\omega_{02})}{(\omega-\omega_{02})^2+\Delta\omega_2^2} + C_2 + \frac{A_3\Delta\omega_3^2 + B_3\Delta\omega_3(\omega-\omega_{03})}{(\omega-\omega_{03})^2+\Delta\omega_3^2} + C_3$] the resonance frequency and linewidth of these three coupled modes can be obtained. The results have been plotted as symbols in Fig. 3.13 (a) and (b), respectively. The red, green, and blue symbols correspond to

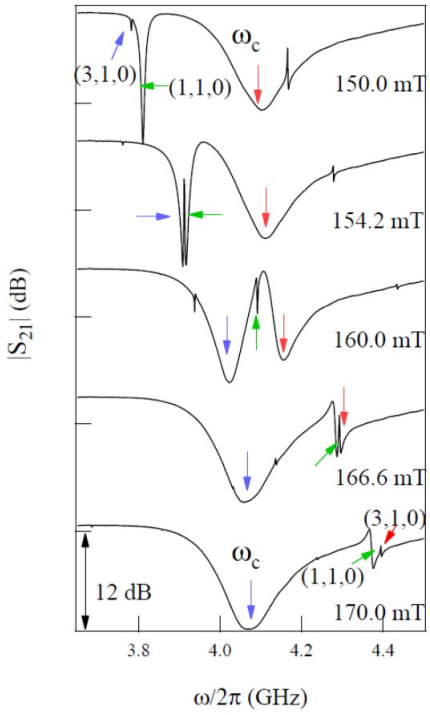

Figure 3.12: (Offset for clarity) Plot of the measured transmission spectra as a function of frequency shows the coupling between the two magnetostatic modes of YIG and the SRR cavity mode at different applied magnetic fields.

the highest, intermediate and lowest frequency modes as identified using the same coloured arrows in Fig. 3.12. The dominant anti-crossing shown in Fig. 3.13 (a) corresponds to the generation of the CMP at 160.0 mT due to the cavity photon-magnon coupling between the cavity mode and the (1,1,0) mode. The (3,1,0) mode does not couple with the cavity mode and simply passes through it but undergoes anti-crossing twice with the lower and upper branches of the CMP at 154.0 and 166.5 mT as shown by the insets. Figure 3.13 (b) shows the corresponding linewidth evolution of the cavity mode and the (1,1,0) and (3,1,0) modes.

The coupling between the cavity mode and the magnetostatic modes can be described by extending the 2 x 2 matrix based on the two coupled classical harmonic oscillators model, described in the Theory section, to a 3 by 3 matrix model that contains three coupled oscillators. To do so, an oscillator with resonance frequency ω_c and damping β which represents the cavity mode, is connected to another oscillator with resonance frequency ω_1 and damping α via a spring with coupling

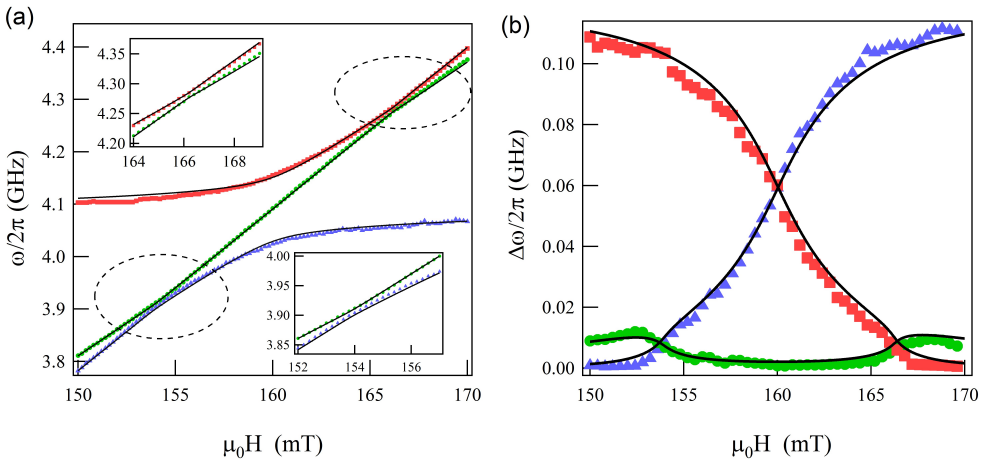

Figure 3.13: Experimentally (symbol) and analytically (solid line) obtained (a) resonance position and (b) linewidth of the coupled magnetostatic modes and the SRR cavity mode plotted as a function of the applied magnetic field

constant κ. This oscillator represents the (1,1,0) magnetostatic mode which is in turn coupled via a coupling constant g to the oscillator that represents the (3,1,0) mode with resonance frequency ω_2 and damping α_2. The equation of motion for this system can be written in a matrix format as $\Omega A = F$ where

$$\Omega = \begin{bmatrix} \omega^2 - \omega_c^2 + i\beta\omega\omega_c & -\kappa\omega_c^2 & 0 \\ -\kappa\omega_c^2 & \omega^2 - \omega_1^2 + i\alpha\omega\omega_c & -g\omega_c^2 \\ 0 & -g\omega_c^2 & \omega^2 - \omega_2^2 + i\alpha_2\omega\omega_c \end{bmatrix}, \tag{3.10}$$

$F = (-f, 0, 0)$ and $A = (A_c, A_1, A_2)$. Here A_c, A_1, and A_2 are amplitudes of oscillation for the different oscillators and f is the driving force acting on the oscillator representing the cavity mode. Since, the (3,1,0) mode simply passes through the cavity mode, the coupling between them is assumed to be zero. The damping for the cavity mode β has been normalised with respect to the cavity resonance frequency ω_c. Its value can be calculated by fitting the experimental data for the cavity resonance measured at $\mu_0 H = 0$. The value of β thus obtained is 0.058. It is assumed that resonance frequency of the magnetostatic modes varies linearly with the applied magnetic field and that their damping parameters α and α_2 remain the same. The value of $\alpha = 0.0009$ and

$\alpha_2 = 0.0002$ was calculated previously from the transmission line measurement of the YIG sphere in Section 3.2.2. The real and imaginary part of the determinant of Ω corresponds to the resonance frequency and linewidth of the coupled modes, respectively.

Thus, by using κ and g as fitting parameters, the theoretical result obtained has been plotted as a solid in line in Fig. 3.13 (a) and (b), respectively. The values of g and κ thus obtained are 0.0049 and 0.04, respectively. The g calculated in this case is slightly higher than the one calculated previously (Section 3.2.2 where $g = 0.0019$) using a transmission line. This might be due to the difference in wave configuration in a microwave transmission line and the SRR cavity. Furthermore, the lineshape of the modes cannot be fitted appropriately using this model. This may be due to the fact that the lineshape of the varactor loaded SRR cavity is not pure Lorentzian or due to the simplicity of the current model. Nonetheless, the frequency dispersion and the linewidth of the modes can be well fitted by using the 3 x 3 classical harmonic oscillator model, as shown by Fig. 3.13 (a) and (b), respectively which reinforces the usefulness of this model in describing multi-mode coupling.

3.2.4 Demonstration of Voltage Control of the Cavity Photon-Magnon Coupling

The previous section describes the experimental results obtained using the traditional method that involves using the applied magnetic field to control the cavity photon-magnon coupling. However, since the resonance frequency of the varactor loaded SRR cavity can be easily and continuously tuned, the coupling between the cavity photons and magnons can also be studied by changing the voltage applied to the SRR cavity. To demonstrate this experimentally, the applied magnetic field was fixed at 152.5 mT such that resonance frequency of the magnetostatic modes was fixed and the applied voltage was tuned from 6.5 V to 15 V.

Figure 3.14 shows a plot of the transmission spectra as a function of frequency measured at different values of voltage applied to the SRR cavity. As shown in the figure, as the applied voltage is increased, the cavity mode (indicated by the red arrow) approaches the (1,1,0) mode

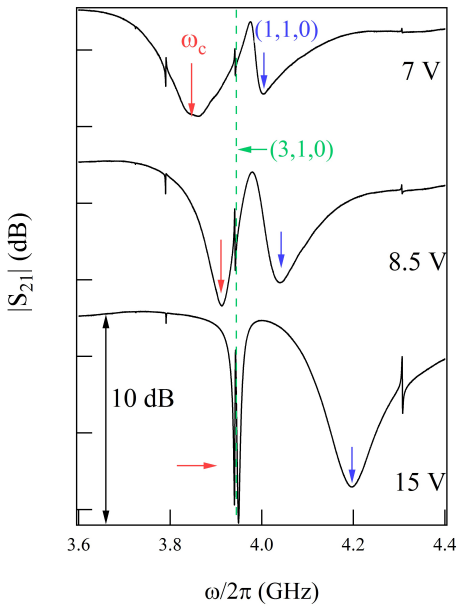

Figure 3.14: (Offset for clarity) Plot of the measured transmission spectra as a function of frequency shows the coupling between the two magnetostatic modes of YIG and the SRR cavity mode at different applied voltages.

(indicated by the blue arrow) at 8.5 V. Furthermore, a decrease in the cavity mode linewidth can also be seen by tuning the applied voltage. This effect is due to the linewidth exchange between the cavity mode and the (1,1,0) magnetostatic mode which shows that hybridised cavity photon-magnon quasi-particles can be generated by simply tuning the applied voltage. This figure also shows that resonance frequency of the (3,1,0) mode (indicated by the green dashed line) remains fixed. This is because of the fact that the (3,1,0) mode does not couple with the cavity mode. However, the amplitude of this mode changes with the applied voltage as it undergoes magnetic coupling with a branch of the CMP generated due to the coupling between the cavity mode and the (1,1,0) mode.

By continuously tuning the applied voltage from 6.5 V to 15 V, the transmission through this system can be measured and the resonance frequency of the modes has been plotted as a function of voltage in Fig. 3.15. For simplicity, the (3,1,0) mode has been omitted as the resonance frequency of this mode does not vary with the applied voltage. In this figure, the uncoupled resonance frequency dispersion of the cavity mode [same as Fig. 3.6 (b)] and the (1,1,0) mode has also been

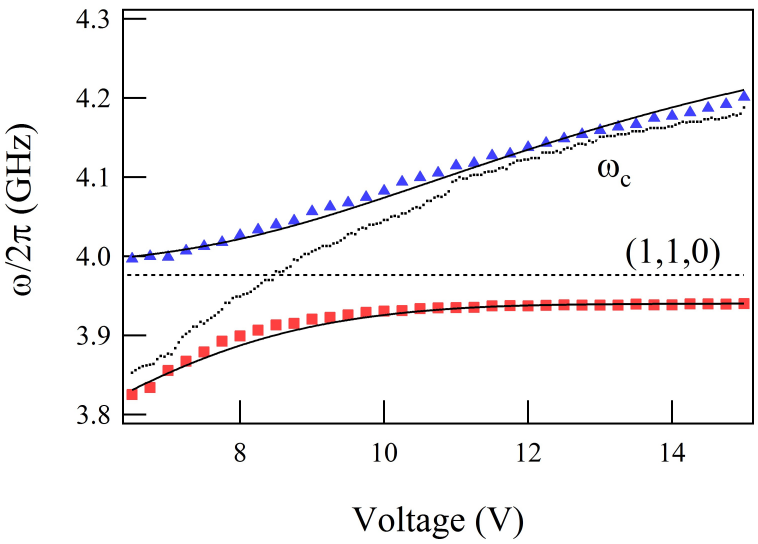

Figure 3.15: Experimentally (symbol) and analytically (solid line) obtained resonance position of the SRR cavity mode and the (1,1,0) mode plotted as a function of the applied voltage. The dotted lines shows the uncoupled resonance frequency of the cavity mode and the (1,1,0) mode.

plotted as dotted lines. The anti-crossing between the cavity mode and the (1,1,0) mode due to the generation of CMP can be clearly seen at around 8.5 V. The resonance frequency of these two coupled modes can also be calculated using the 3 x 3 matrix model [Eq. (3.10)] and the result has been plotted as a solid line in Fig. 3.15 where again there is good agreement between the experimental and calculated results.

Therefore, this varactor loaded SRR cavity not only gives an additional degree of freedom to study the cavity photon-magnon coupling (by tuning the applied voltage to tune the cavity resonance frequency) but also has the advantage of being planar and thus being better suited for practical applications. The quality factor of this cavity could be further improved by using high temperature superconducting substrates/films for fabrication which would make this electrically tunable cavity even more suitable for potential practical applications. This work has been published in the Applied Physics Letters.[50]

3.3 Non-Resonant Radiation Damping in Cavity Magnon Polariton Systems

As discussed in the previous section, planar cavity photon-magnon coupling systems are more suitable for the various potential practical applications that have been proposed[13, 39]. However, in a planar system, a quantitative simulation is essential where the radiation damping must be considered.

Radiation damping is the loss of energy due to the emission of radiation[51]. This radiation can take different forms in different coupled systems. For example, in vibrating systems the energy is radiated in the form of sound due to acoustic radiation damping[52] whereas in coupled surface plasmon polariton systems, modification of the radiative decay due to the coupling between optical excitation leads to generation of super and sub radiance states[53]. Radiation damping in magnetic resonance experiments has been studied for decades[54] and has been attributed to the generation of the magnetic dipole radiation due to the precession of dipole moments[55, 56, 57]. This precession is excited due to the inductive coupling between the waveguide and the magnetic sample[58] and can be calculated using either the photon-magnon Hamiltonian[56, 59], or the Landau-Lifshitz equation[56] and Bloch's equation[54].

However, a simpler theoretical formalism for this magnetic radiation damping can be found by using the CMP physics. As described in the Theory section of this thesis, the CMP physics can be modelled by using a 2 x 2 matrix model that has three important parameters, the coupling strength (κ) measured at the cavity resonance frequency (ω_c) and the uncoupled damping parameters of the cavity mode (β) and the magnon mode (α). This model can well explain the mode anti-crossing (that represents the generation of CMP) and the resonant radiation damping that leads to the linewidth exchange between the cavity photon-like and magnon-like hybridized modes. However in planar cavity systems, the YIG sphere that generates the magnon mode may lose energy to the surroundings, especially in the weak coupling regime, due to the effect of the non-resonant radiation damping. Thus, for a complete theoretical description of the CMP physics,

it is important to consider all the sources of damping for the YIG sphere and accordingly modify the 2 x 2 matrix model.

3.3.1 Modelling the Non-Resonant Radiation Damping

In a planar cavity photon-magnon system, the damping of the YIG sphere consists of two parts: the damping that arises due to the exchange in energy between the YIG sphere and the cavity due to the coupling between them, and the damping that arises due to the loss of energy by the YIG sphere to the environment due to magnetic dipolar radiation. In order to simultaneously describe the two sources of radiation damping, the 2 x 2 matrix model can be extended by adding a non-resonant damping term that represents the open space. The resulting 3 x 3 matrix equation is given by $f = \Omega A$ where $f = (-f, 0, 0)^T$, $A = (A_c, A_m, A_e)^T$ and

$$\Omega = \begin{bmatrix} \omega - \omega_c^2 + i\beta\omega\omega_c & -\kappa\omega^2 & 0 \\ -\kappa\omega^2 & \omega - \omega_m^2 + i\alpha\omega\omega_m & -\rho\omega^2 \\ 0 & -\rho\omega^2 & \omega^2 + i\xi\omega^2 \end{bmatrix}. \tag{3.11}$$

Here, f is the driving force acting on the system, and A_c, A_m, A_e are the amplitudes of oscillations for the resonators representing the cavity photon, magnon, and the environment, respectively. κ represents the coupling between the cavity mode and the magnon mode whereas ρ represents the coupling between the magnon mode and the environment. ω_m denotes the resonance frequency of the magnon mode that can be determined from the Kittel's equation $\omega_m = \gamma(H + H_0)$, whose parameters γ and $\mu_0 H_0$ can be determined experimentally. Since the environment has no obvious resonance, it has been represented as a non-resonant term with a microwave energy dissipation rate of ξ. Therefore, in this case the environment can refer to any non-resonant damping channel. The

transmission through this system is proportional to A_c[18] and is given by

$$S_{21} \propto \frac{1}{(\omega^2 - \omega_c^2 + i\beta\omega\omega_c) - \dfrac{\kappa^2\omega^4}{(\omega^2 - \omega_m^2 + i\alpha\omega\omega_m) - \dfrac{\rho^2\omega^4}{\omega^2 + i\xi\omega^2}}} \tag{3.12}$$

Based on the 3 x 3 matrix, an equivalent phenomenological RLC circuit model can be built to quantitatively describe this system as shown in Fig. 3.16. In this figure, the series RLC circuit consisting of R_c, L_c and C_c represents the cavity mode that is inductively coupled via an inductance M with the YIG sphere, which is represented by another series RLC circuit that consists of R_m, L_m and C_m. The YIG sphere is then in turn coupled to the environment through an inductor with inductance M'. Since the environment functions as a non-resonant absorber, it can be represented using an inductively coupled circuit with resistance R' and inductance L'[60]. Therefore, all the parameters in Eq. (3.12) can be related to the RLC circuit model as $\omega_c = 1/\sqrt{R_c L_c}$, $\omega_m = 1/\sqrt{R_m L_m}, \alpha = R_m C_m, \beta = R_c L_c\ \kappa = M/\sqrt{L_m L_c}, \rho = \kappa\sqrt{L_c/L'}$ and $\xi\omega = R'/L'$. Thus, the transmission through this RLC circuit has the same form as Eq. (3.12).

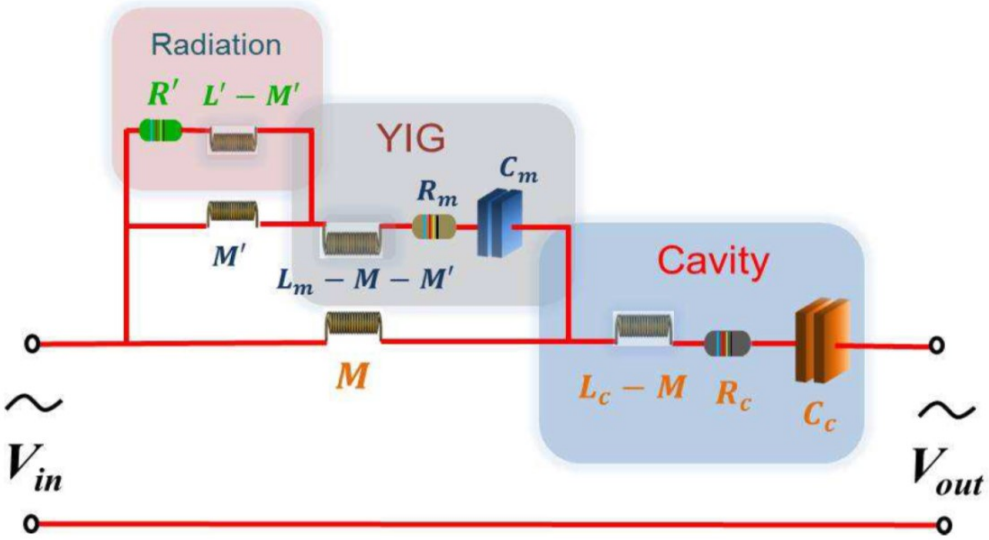

Figure 3.16: Schematic diagram of the phenomenological RLC circuit model that can be used to describe the non-resonant radiation damping in coupled CMP systems.

The impact of coupling between the magnon mode and the environment (ρ) on the coupled CMP system can therefore be studied by expanding the denominator of the second term in Eq. (3.12). For small value of ρ the denominator can be written as $\omega^2 - \omega_m'^2 + i\Delta\omega_m'\omega$ where

$$\omega_m' \simeq \omega_m(1 + \frac{\rho^2}{2(1+\xi^2)}) \tag{3.13}$$

and

$$\Delta\omega_m' = \alpha\omega_m' + \frac{\rho^2\xi\omega}{1+\xi^2} \tag{3.14}$$

The above equations show that when $|\omega_c - \omega_m| \gg \alpha\omega_m, \beta\omega_c$ i.e. the cavity and magnon resonance frequencies are far away from each other, the coupling between the magnon mode and the environment would produce two simultaneous effects on the magnon mode: its resonance frequency will be blue-shifted and there will be an additional linewidth broadening. These two effects are found to be directly proportional to ρ^2.

3.3.2 Experimental Verification of the Non-Resonant Radiation Damping Model

In order to experimentally verify the above described theoretical predictions, the planar cavity shown in Fig. 3.17 was fabricated on a 1.5 mm thick PCB board with a Rogers RT/duroid 5880 (ϵ_s = 2.2) substrate. The length and width of the cavity is 31 mm and 2 mm, respectively. The damping factor of this planar cavity (β) can be optimized by tuning the two gaps between the stripline cavity, port 1, and port 2. Here, the gap was chosen to be 1.6 mm. The microwave transmission through this planar cavity can be measured by connecting it to a VNA and the result is shown in Fig. 3.18(a). The resonance frequency (ω_c) of the cavity is measured to be at 3.45 GHz with a damping factor of $\beta = 4.8 \times 10^{-3}$ and a quality factor of approximately 100. The solid line in the figure is the calculated result from Eq. (3.12) with $\kappa, \rho = 0$.

To study the radiation damping of a coupled CMP system, a 1 mm diameter YIG sphere was placed in a sample holder that was kept slightly above the surface of the planar cavity. This YIG

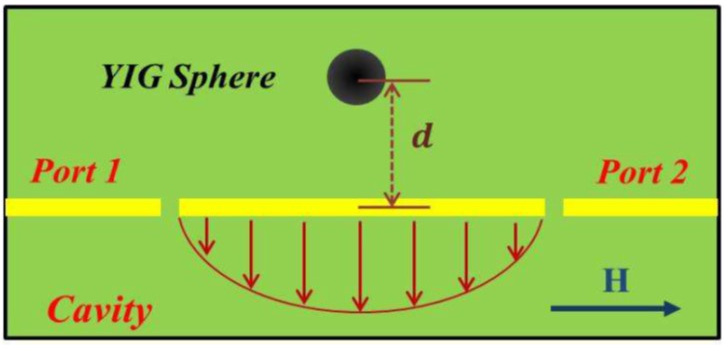

Figure 3.17: Schematic diagram of the fabricated cavity with a 1 mm diameter YIG sphere that was placed above its surface.

sphere had a gyromagnetic ratio of $\gamma = 27.5 \times 2\pi\mu_0$ GHz/T, an anisotropy field of $\mu_0 H_a = 1.7$ mT and a damping factor of $\alpha = 2 \times 10^{-4}$ that were determined experimentally. The stripline cavity was attached to a Velmex x-y-z stage which could freely move in all directions. Therefore, using this experimental set-up, the coupling strength between the cavity and the YIG sphere could be continuously tuned while the external applied magnetic field on the YIG sphere remained the same. The microwave transmission through this system was then measured at 123 mT when the separation between the planar cavity and the YIG sphere (d) was fixed at 2 mm. The result has been plotted in Fig. 3.18(b) which corresponds to the case that the resonance frequency of the cavity and the magnon mode is matched. In this strongly coupled case, the energy exchange between the cavity photon and the YIG magnon is dominant therefore the energy radiated by the YIG sphere to the environment can be ignored (i.e. $\rho \simeq 0$). The cavity photons couple with the magnons to generate the Rabi gap of CMP ($\Delta\omega_{gap}$) which is proportional to the coupling strength κ between them. In this case, κ is determined to be 0.0182 from $\Delta\omega_{gap} = \kappa\omega_c$[18] and the calculated result from Eq. (3.12) has been plotted as a solid line in Fig. 3.18(b) where good agreement between the experimental and calculated results can be seen.

In order to experimentally determine the relationship between κ and ρ, the variation of κ with distance (d) was first determined. This was achieved by measuring a series of transmission spectra at 123 mT by continuously varying the cavity-YIG separation. Figure 3.19 shows four typical

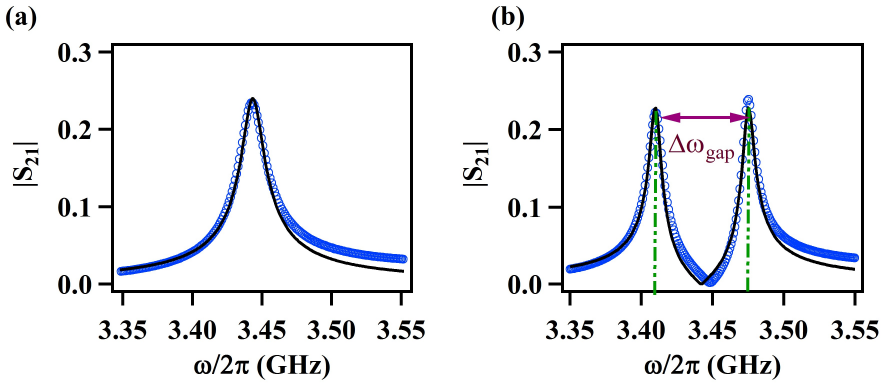

Figure 3.18: Measured (symbol) and calculated (solid line) microwave transmission plotted as a function of frequency (a) without the YIG sphere and (b) with the YIG sphere at a distance of 2 mm from the cavity. The red arrow indicates Rabi gap of CMP ($\Delta\omega_{gap}$) generated due to the cavity photon-magnon coupling.

transmission spectra measured when the separation between the YIG sphere and the cavity was 2, 3, 4 and 5 mm. The spectra shown in this figure have been offset for clarity and clearly show a decrease in the Rabi gap of CMP or the coupling strength as the distance between the YIG sphere and the cavity increases. From these spectra, the coupling strength κ can be determined and has been plotted as a function of 1/d in Fig. 3.20.

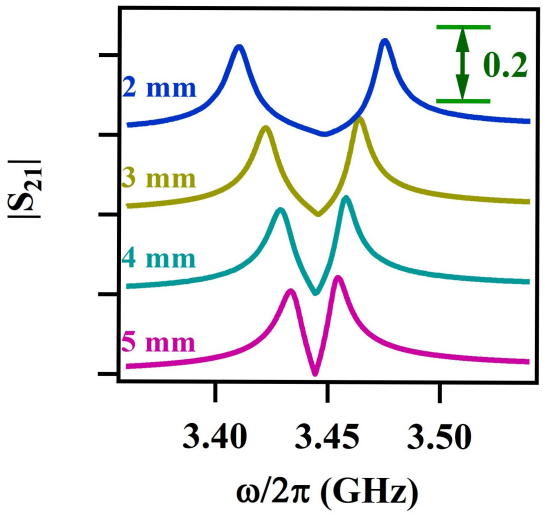

Figure 3.19: Typical transmission spectra measured at different values of separation between the YIG sphere and the cavity.

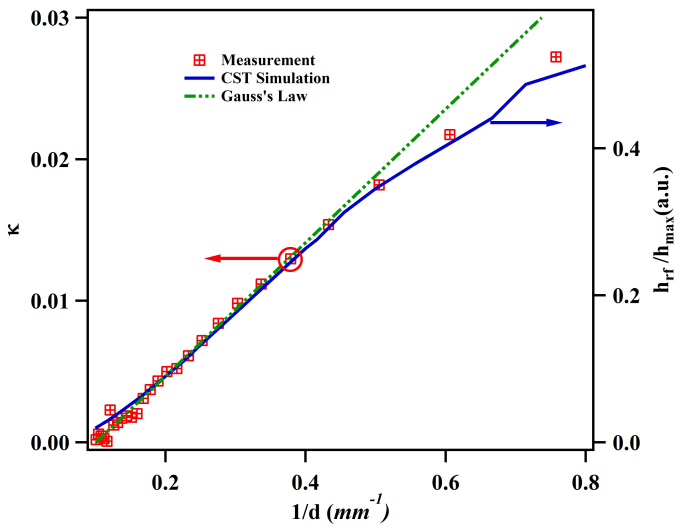

Figure 3.20: Measured photon-magnon coupling strength (symbol), simulated amplitude of microwave magnetic field generated by the cavity (solid line) and the result from Gauss' Law (dashed green line) plotted as a function of inverse of the distance from the cavity.

In this experiment $\kappa \propto \eta \propto h_{rf}/h_{max}$ where η is the overlap coefficient[15], h_{max} is the maximum microwave magnetic field generated by the stripline cavity (which is fixed for a fixed input microwave power) and h_{rf} is the amplitude of microwave magnetic field at the position of the YIG sphere. To verify this distance dependence of the coupling strength, the microwave magnetic field generated by the stripline cavity was simulated as a function of the distance (d) from the cavity using the computer simulations technology (CST) software. The result has been plotted as a solid line in Fig. 3.20 and shows that h_{rf}/h_{max} is also inversely proportional to d. This observation can also be explained theoretically by using Gauss' Law which states that the magnetic field generated by a current carrying wire of a finite length at any point is inversely proportional to the distance from the wire. The result calculated from Gauss' Law has been plotted as a green dashed line in Fig. 3.20. This result shows some deviations when the YIG sphere is very close to the cavity such that the separation between them is comparable to the actual size of the YIG sphere. Nonetheless, good agreement between the theoretical, experimental and simulated results can be seen when the separation between the YIG sphere and the cavity is greater than the size of the YIG sphere.

To verify the theoretical predictions made in the previous section regarding the effect of the

non-resonant radiation damping on the resonance frequency and linewidth of the uncoupled magnon mode, the applied magnetic field was set at 133 mT. The magnon resonance frequency was therefore at 3.71 GHz which is far away from the cavity resonance frequency of $\omega_c/2\pi = 3.4$ GHz. In this case, since $|\omega_c - \omega_m| \gg \alpha\omega_m, \beta\omega_c$ the effect of the non-resonant radiation damping should become apparent. To study these effects a series of transmission spectra were measured at different separations between the YIG sphere and the planar cavity and some typical spectra have been plotted in Fig. 3.21. The figure shows that the resonance frequency and linewidth of the magnon mode varies with the separation due to the coupling effect. Furthermore, the magnon signal lineshape changes from a transmission maximum to a transmission minimum as the distance between the YIG sphere and the cavity is increased. This variation can be explained as follows. Generally, in a waveguide measurement of the YIG ferromagnetic resonance, there is minimum transmission at the resonance frequency because of absorption of the microwave energy by the YIG sample. The transmission maximum that is observed in Fig. 3.21 shows that at small values of separation between the YIG sphere and the cavity, the hybridized mode generated due to the cavity photon-magnon coupling is dominated by the signal from the cavity mode. As the separation increases, the hybridized mode becomes dominated by the signal from the magnon mode and the lineshape changes to being a transmission minimum. The measured transmission signal can be fitted by using a combination of symmetric and anti-symmetric Lorentzian lineshapes [Eq. 3.9][46] and the result has been plotted as a solid line in Fig. 3.21.

From the fitting results, the resonance frequency and linewidth can be obtained and have been plotted as a function of the square of the coupling strength κ^2 [obtained from Fig. 3.20] in Fig. 3.22(a) and (b), respectively. As shown by the figures, both the resonance frequency and linewidth of the magnon mode vary linearly with κ^2. The dashed lines are the result obtained from Eq. (3.12) with $\rho = 0$ which corresponds to the case that the YIG radiates no energy to the environment. In this case, the 3 x 3 model reverts back to the 2 x 2 model that has been previously used to describe the cavity photon-magnon coupling. As shown by the figures, even though the calculated resonance frequency and linewidth vary linearly with κ^2, there exists a significant difference between the

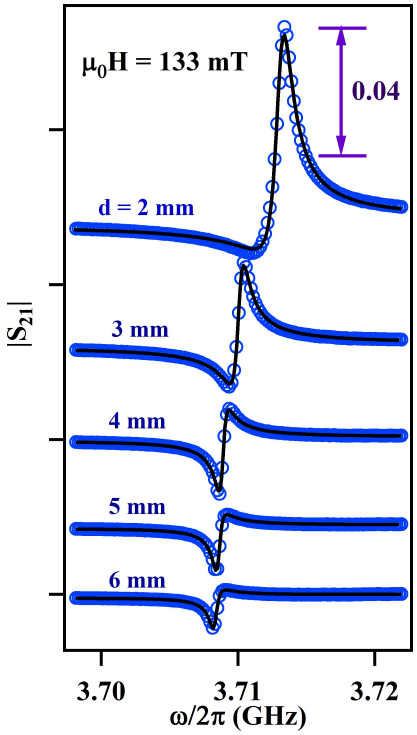

Figure 3.21: Typical transmission spectra measured (symbol) at different values of separation between the YIG sphere and the cavity. The solid line is the fitting result obtained by using a combination of symmetric and anti-symmetric Lorentzian lineshapes [Eq. (3.9)].

theoretical and experimental results especially for the linewidth. This deviation can be resolved by taking into account the non-resonant radiation damping by using the 3 x 3 model proposed in the previous sub-section. The results calculated from Eq. (3.12) have been plotted as a solid line with the open space dissipation rate $\xi = 0.33$ and the coefficient $\rho/\kappa \simeq 1$. This linear relationship between ρ, κ and the magnon mode linewidth implies that the stronger the photon-magnon coupling the larger the linewidth of the magnon mode.

Using the experimentally determined values of ξ and ρ in the phenomenological RLC circuit model, it can be obtained that $M' \sim M, L' \sim L_c$ and the resistance R' of the open space shows a frequency variation given by $R' = \xi\omega L_c$. Therefore, all the parameters of the RLC circuit have been determined and it can now be used for simulation purposes.

Hence, the conventional 2 x 2 matrix model used to explain the cavity photon-magnon coupling has been modified to include a non-resonant damping term to take into account the energy lost by

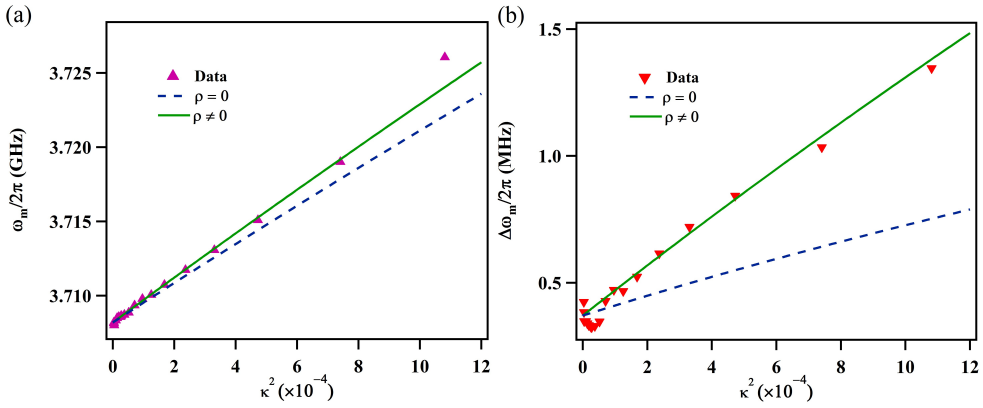

Figure 3.22: Experimentally measured (symbol) and theoretically calculated (a) resonance frequency and (b) linewidth variation using $\rho \neq 0$ (solid line) and $\rho = 0$ (dashed line).

YIG to the environment. The effect of this energy loss becomes apparent in a planar cavity system when the resonance frequency of the cavity photon and magnon modes are mismatched. In this case, both the magnon resonance frequency and linewidth show a linear variation with the cavity photon-magnon coupling strength which can be easily explained by the 3 x 3 matrix model and simulated using the phenomenological RLC circuit model. This matrix model provides a simple and precise explanation of the radiation damping induced by the coupling effect and it can be easily extended to describe other many-body systems that include both resonant and non-resonant objects. This theoretical modelling and experimental realization of the non-resonant radiation damping in planar cavity photon-magnon systems may help in the design and adaptation of these systems for potential practical applications. This work has been published in the Applied Physics Letters[61].

3.4 Pseudo Cavity Magnon Polariton Device for Voltage Control of Electromagnetically Induced Transparency

Apart from the potential practical applications of the cavity photon-magnon coupled systems in developing quantum transducers[17] and long lifetime multi-mode quantum memories[16], it has been shown that in 3-D cavities the CMP coupling leads to electromagnetically induced transparency (EIT)[15]. In this section, the development of a 2-D pseudo CMP system that can be used to achieve tunable EIT is described and an LCR circuit that can be used to precisely simulate this observation is proposed.

EIT is an effect that renders an otherwise opaque medium transparent over a narrow frequency window and is accompanied by a sharp change in refractive index[62]. EIT was first observed in alkali vapours[63] and occurs due to the destructive interference between two different excitation pathways[64]. These pathways are often labelled as the 'bright' and the 'dark' mode and correspond to the mode that can and cannot be directly excited by the incident electromagnetic radiation[65, 66]. These modes are usually generated due to an asymmetric excitation of the system. For example in a three-level atomic system which is often used to study EIT[62], the transition of the atom from the ground state to the excited state which is directly excited by the probe beam is referred to as the 'bright mode'. Whereas, the transition of the atom from the meta-stable state to the excited state which is not directly excited by the probe beam is referred to as the 'dark mode'.

The observation of EIT in alkali vapours could not be used for the development of practical applications because this effect requires high power lasers, high magnetic fields and cryogenic temperatures[62]. But, it was soon realized by researchers that this quantum effect has many classical analogues such as coupled mechanical oscillators which led to the implementation of this effect in coupled optical resonators and photonic crystal waveguides[62]. Since these structures extend along the direction of propagation of waves, they imposed a restriction on the minimum dimension of the medium. This restriction was overcome by using metamaterials.

In 2007, the first observation of EIT in metamaterials was made by Fedotov et al[67], follow-

ing which continuous research in this area has led to the development of various metastructure designs that can demonstrate EIT like features in the mid-infrared, microwave, optical, and THz region of the frequency spectrum[66, 68, 69, 70, 71, 72, 73, 74, 75, 76, 77, 78]. Several potential applications for these metamaterial based systems have also been proposed such as optical buffering, compact delay lines, high sensitivity refractive index sensors and data storage due to the permittivity dependent slow light behaviour associated with EIT[62, 70]. Apart from further developing potential applications for this phenomenon, the current focus of researchers has been on developing metamaterial systems that offer the ability to control EIT. Passive control of EIT has been achieved by varying the design parameters associated with the metamaterial design such as the distance between the meta-structures or the resistance of the meta-structures[62, 73]. However, to achieve the full potential of this non-linear effect and in order to develop further practical applications such as designing dynamic filters, phase shifters and switch devices, it is important to achieve active control of EIT.

Active control of metamaterial EIT has so far being achieved by fabricating the sample on a compressible/stretchable substrate and applying an external force that would change the separation between the different elements of the meta-structure or by temperature control of the resistance of the meta-structure fabricated on superconducting substrates[79, 80, 81, 82]. Furthermore, in 3-D cavities the EIT effect due to the cavity photon-magnon coupling can be actively controlled by tuning the applied magnetic field. However, from the perspective of device application, the external applied magnetic field used to alter the energy exchange efficiency or the coupling strength between the cavity mode and the magnon mode is not favourable. Thus, the motivation behind the experiments that are described in the following sections was to develop simple alternative methods to achieve active mechanical and electrical control of the EIT effect in metamaterial based pseudo-CMP systems.

3.4.1 Transmission Line Model for Pseudo Cavity Photon-Magnon Coupling

As described in previous section, the study of metamaterials[22, 21] has allowed the development of non-magnetic conducting materials that can be designed to provide a magnetic response at microwave frequencies. Inspired from this work, a 2-D artificial CMP system was created by integrating an artificial magnetic resonator with an on-chip cavity resonator. The cavity mode and the artificial magnon mode are created by using a cut-wire resonator and a rectangular SRR, respectively that are mutually coupled with each other. The rectangular shape of the SRR ensures maximum coupling between the cut-wire and the SRR. Here, the cut-wire resonator acts as a 'bright mode'; whereas, the SRR acts as a 'dark mode' as it cannot be directly excited by the incident microwaves. The microwave magnetic field produced due to the microwave current flowing in the cut wire induces a microwave current in the SRR. Thus, an effective magnetic response is produced by the SRR which can be characterized by its resonant permeability[21] due to which the SRR can be used to mimic the magnetic response of an YIG sample.

Similar to that of the cavity photon-magnon coupling, the response of the pseudo CMP can be described by using 5 parameters, the cavity resonance frequency (ω_c), the pseudo-magnon resonance frequency (ω_s), the damping of the cavity mode and the magnon mode β and α, respectively and the coupling strength between them (κ). To quantify these parameters from the microwave transmission that is measured for this pseudo-CMP system, the transmission line model for coupled LCR circuits can be used.

In order to model the cavity and the pseudo magnon modes in terms of LCR circuits, the transmission line models proposed in Ref. [83] have been used to separately describe the cut-wire and the SRR, respectively. As shown by the insets of Fig. 3.23 (a) and (c), the cut wire and the SRR can be represented as a series and parallel LCR circuits whose impedance is given by

$$Z_c = R_c + i(\omega L_c - \frac{1}{\omega C_c}), \tag{3.15}$$

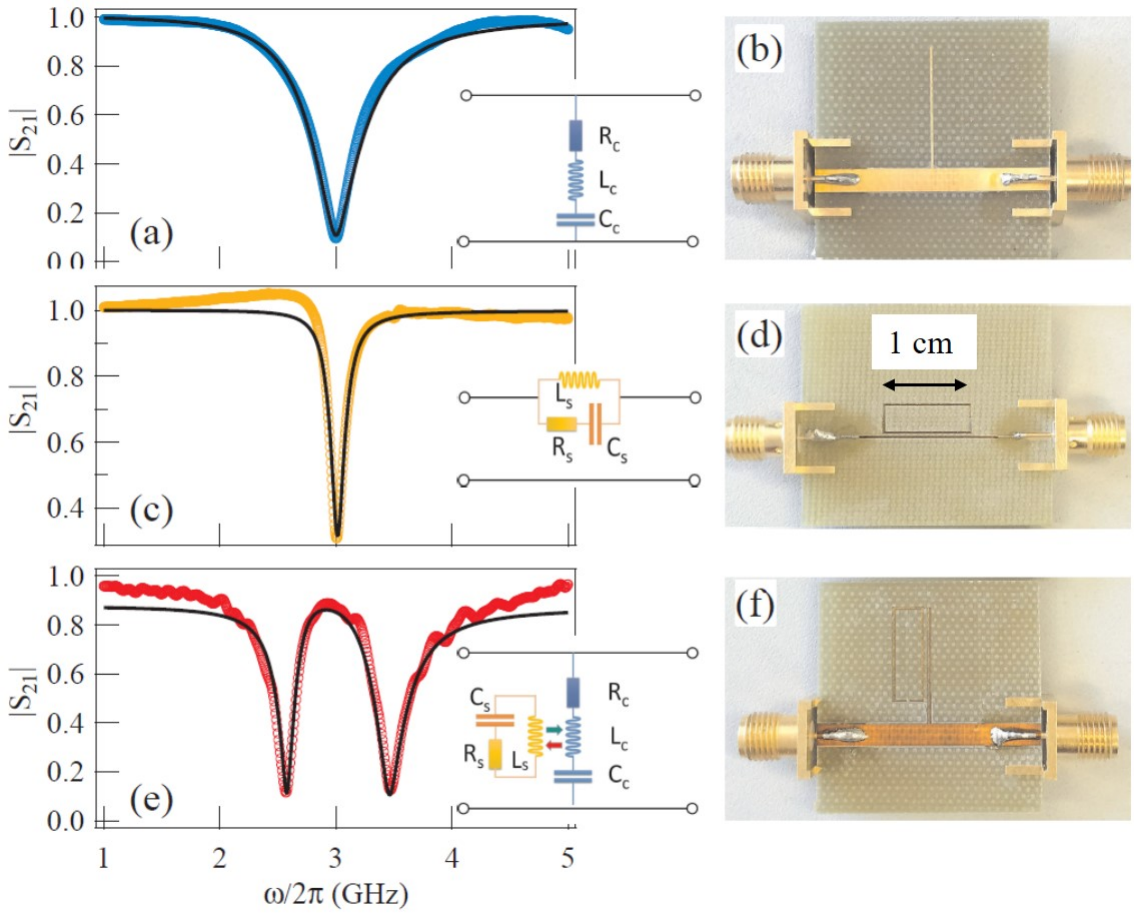

Figure 3.23: Experimentally measured (symbols) and analytically calculated (solid lines) transmission curves for (a) the cut wire resonator connected to a 50 Ω transmission line, (c) the SRR excited by a 150 Ω transmission line, and (e) the coupled cut wire and SRR separated by a distance of 2.7 mm. The insets show the corresponding equivalent LCR circuits. (b), (d) and (f) are photographs of the fabricated microwave devices.

and

$$Z_s = \frac{\omega L_s - R_s \omega^2 L_s C_s}{1 - \omega^2 L_s C_s + i\omega C_s R_s}, \tag{3.16}$$

respectively. Here the subscripts 'c' and 's' are used to denote the parameters that correspond to the cut wire and the SRR, respectively. The LCR circuit for the SRR can also be equivalently represented as a capacitance(C_s') in parallel with an inductance (L_s') that is in series with a resistance (R_s'). In this case, the impedance of the circuit will be given by $Z_s = \frac{R_s' + i\omega L_s'}{1 - \omega^2 L_s' C_s' + i\omega C_s' R_s'}$. The values of the parameters will be slightly different in this case, but the response of the two circuits

will be the same which implies that these two representations can be used interchangeably. Using the ABCD matrix and the conversion formula [Eq. (3.3)], the transmission (S_{21}) parameter can be obtained as

$$S_{21} = \frac{2Z_c}{2Z_c + Z_0}, \tag{3.17}$$

and

$$S_{21} = \frac{2Z_0}{2Z_0 + Z_s} \tag{3.18}$$

for the cut wire resonator and the SRR, respectively. Here Z_0 is the characteristic impedance of the transmission line.

In order to describe the combination of the two resonators for the observation of pseudo-CMP, the circuit shown in the inset of Fig. 3.23(e) was used in which the interaction between the two resonators is modelled using a mutual inductance M between the inductors L_c and L_s. This interaction can also be described by using a transformer that links the magnetic flux generated by the cut-wire resonator to the inductor of the SRR. From the net impedance of this circuit, the S_{21} parameter can be written as

$$S_{21} = 1 - \frac{\dfrac{Z_0 \Delta\omega_c}{Z_0 + 2R_c}}{i(\omega - \omega_c) + \beta + \dfrac{\kappa^2}{i(\omega - \omega_s) + \Delta\omega_s}}. \tag{3.19}$$

Here, $\omega_c = \dfrac{1}{\sqrt{L_c C_c}}$, $\omega_s = \dfrac{1}{\sqrt{L_s C_s}}$, $\Delta\omega_c = \dfrac{C_c \omega \omega_c^2 (R_c + Z_0/2)}{\omega + \omega_c}$, and $\Delta\omega_s = \dfrac{C_s R_s \omega_s^2 \omega}{\omega + \omega_s}$ are the resonance frequency and linewidth of the cut wire and SRR, respectively. The coupling strength $\kappa = \omega^2 M \omega_c \omega_s \sqrt{\dfrac{C_c C_s}{(\omega + \omega_c)(\omega + \omega_s)}}$ is linearly dependent on the mutual inductance M. When $\omega \sim \omega_c \sim \omega_s$, it can be found that $\Delta\omega_c \sim \dfrac{R_c + Z_0/2}{2L_c}$, $\Delta\omega_s \sim \dfrac{R_s}{2L_s}$, and $\kappa \sim \dfrac{M\omega}{2\sqrt{L_c L_s}}$. The damping of the cut wire and the SRR as well as the coupling strength have a unit of frequency here. The impedance mismatch between the 50 Ω microstrip line and the 150 Ω SRR lines has been ignored for the purpose of simplicity as the focus here is to qualitatively model the response

the coupled cut wire and SRR system. Eq. (3.19) has a similar form as that of the coupled cavity photon-magnon system [as described in the Theory section Eq. (2.3)] which indicates that the artificial CMP has similar physical features.

In order to validate this LCR circuit based transmission line model, the cut-wire resonator, the SRR, and their combination was fabricated on a 1.55 mm thick FR-4 substrate with a copper thickness of 35 μm. Figure 3.23(b), (d), and (f) show photographs of the fabricated microwave devices. The cut-wire resonator was positioned at the center of a 50 Ω transmission line and had a length and a width of 15.1 mm and 0.2 mm, respectively. The SRR was 4 mm in width and 12 mm in length and had a linewidth of 0.2 mm. A 0.2 mm gap was located at the center of the width of the resonator and a 0.2 mm wide 150 Ω transmission line was used to excite its resonance. In Fig. 3.23(f) the gap between the center of the two resonantors is 2.7 mm and the microstrip line has a characteristic impedance of 50 Ω. The transmission response of these fabricated devices was then measured by connecting them to a VNA.

Figure 3.23(a), (c), and (e) shows the measured transmission response plotted as a function of the microwave frequency. As shown by the figures, a transmission minimum at the resonance frequency of 3.0 GHz is observed for both the cut wire and the SRR, respectively; whereas, a transmission maximum centred at 3.0 GHz is obtained when the two resonators are coupled. This transmission response can be explained by the fact that when a cut wire or a SRR is directly excited by microwave radiation flowing through the transmission line, a current is induced in the cut wire (SRR) that produces electric (magnetic) fields. The induced electric (magnetic) field exactly cancels the electric (magnetic) field of the microwave radiation flowing in the transmission line, thereby minimizing transmission at resonance. However, when the cavity mode and the pseudo magnon mode are coupled together and have an identical resonance frequency, the electrodynamic coupling between them leads to the generation of an artificial CMP gap that is centred at the original resonance frequency of the resonators. Hence, a transmission maximum is obtained in this case.

By fitting the experimentally obtained transmission curves for the cut wire and the SRR using

the transmission line models given by Eqs (3.17) and (3.18), the transmission curves obtained have been plotted as a solid line in Fig. 3.23(a) and (c), respectively. The corresponding values of $R_c = 2.87\Omega$, $C_c = 0.499$ pF and $L_c = 5.64$ nH for the cut wire resonator, and $R_s = 0.091\Omega$, $C_s = 8.78$ pF and $L_s = 0.314$ nH for the SRR were obtained from the fitting. Therefore, the transmission spectra for the coupled resonators shown in Fig. 3.23(e) can be calculated by using just one fitting parameter i.e. mutual inductance $M = 0.74$ nH. As shown by the Figs. 3.23(a), (c) and (e) there is good agreement between the experimentally measured and theoretically calculated results using the transmission line models.

3.4.2 Distance Dependence of Coupling Strength

Since the mutual inductance (M) determines the coupling strength κ which characterizes the energy transfer efficiency between the cavity mode and the quasi-particle system[10], it is necessary to understand its physical origin in an artificial CMP system for practical applications. In order to do so, another experiment was performed wherein the distance between the two resonators fabricated as separate chips was tuned in the horizontal direction by using a Velmex x-y-z stage. Figure 3.24 shows a schematic diagram of the experimental set-up in which the cut wire resonator integrated with a 50 Ω transmission line was connected to a VNA whereas the SRR was mounted on the x-y-z stage. The separation between the two chips was less than 20 μm. By tuning the distance between the two resonators along the y-direction, the coupling between them can be changed.

The left panel of Fig. 3.25(a) shows some typical transmission (S_{21}) spectra measured at different values of y-distance between the resonators, whereas the right panel shows the corresponding flux-configuration between the resonators due to the microwave current in the cut-wire resonator. When the SRR is far from the cut wire, the magnetic flux generated by the cut wire cannot excite the SRR's resonance and only the cut wire's resonance is measured at 3.0 GHz. As the distance between the cut wire and the SRR decreases, the amount of magnetic flux through the SRR increases which leads to an increase in coupling strength between the cut wire and the SRR which therefore leads to an increase in frequency range of the transmission window. The coupling strength is

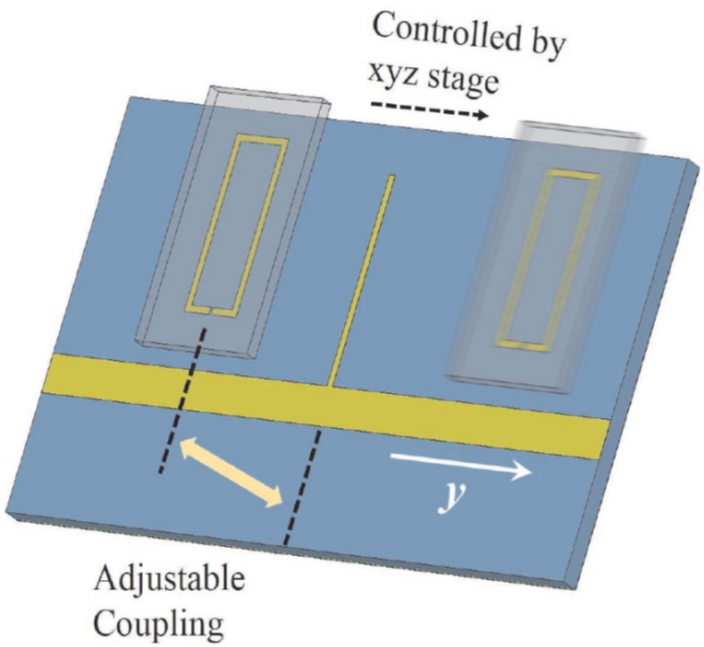

Figure 3.24: Schematic diagram of the experimental set-up used to achieve active tunability of the pseudo-CMP coupling by tuning the distance between the resonators.

therefore maximum when the edges of the cut wire and the SRR are closest without any overlap. However when the cut wire is exactly at the centre of the SRR (y = 0), the cut wire induces equal and opposite amounts of flux in the two arms of the SRR due to which the resonance of the SRR cannot be excited. Therefore, the transmission corresponds to the resonance response of the cut wire alone. However, as soon as the cut wire is no longer at the centre of the SRR, the transmission window reappears. Figure 3.25(b) shows the transmission amplitude mapping obtained by tuning the distance y between the resonators in the horizontal direction. The mapping is symmetric around y = 0 mm.

By fitting the various transmission spectra obtained from the distance tuning experiment using the transmission line model [Eq. (3.19)], the mutual inductance between the resonators can be plotted as a function of distance as shown in Fig. 3.26. This dependence of mutual inductance on the distance between the resonators can be explained by calculating the flux (ϕ) through the SRR due to the microwave current I in the cut-wire as

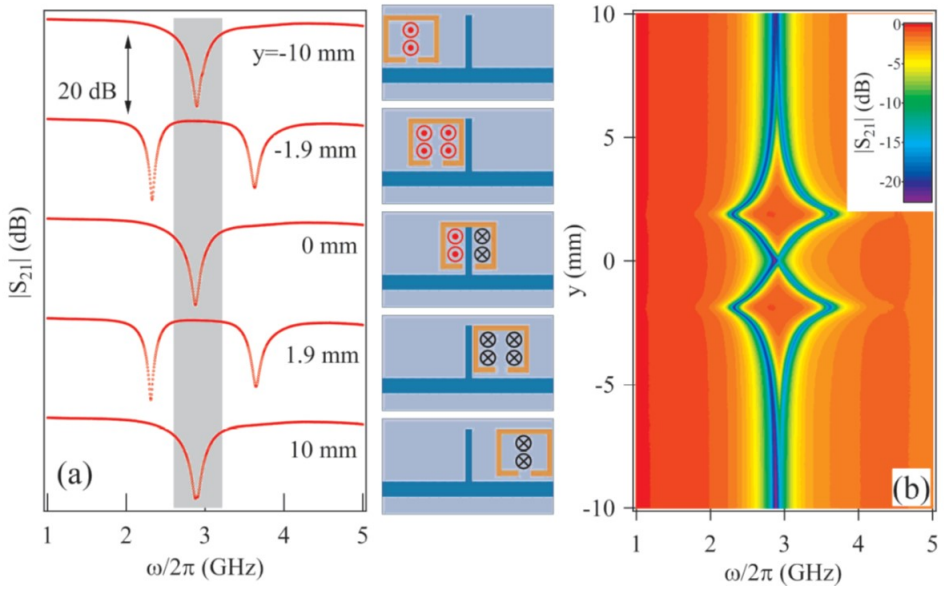

Figure 3.25: (a)The left panel shows typical S_{21} spectra (offset for clarity) obtained at different resonator separations and the right panel shows the schematic diagram of the corresponding measurement configuration along with the amount of flux flowing through the SRR. (b) The S_{21} amplitude mapping result for distance y between the two resonators as a function of frequency.

$$M = \frac{\phi}{I} = \frac{\oint \overrightarrow{B} \cdot \overrightarrow{dA}}{I}, \tag{3.20}$$

where from Gauss' Law $B = \dfrac{\mu_0(\cos\theta_1 + \cos\theta_2)}{4\pi y}$ is the microwave magnetic field produced by the finite length of the cut wire, θ_1, θ_2 are the angles subtended by the two end points of the cut-wire at any point on the SRR located at a distance y from the center of the cut-wire, and A is the area of the SRR. For simplicity, the effect of the substrate of the SRR is neglected and the magnetic field is integrated over the width of the SRR and the result is simply multiplied by the length of the SRR. This theoretically obtained result has been plotted as a solid line in Fig. 3.26 where good qualitative agreement between the experimental and theoretical results can be seen.

Using the experimentally obtained data, the different coupling regimes that are reached (as defined by Zhang et. al[15]) by tuning the y-distance and hence the coupling strength between the cavity mode and the pseudo magnon mode can be classified. As shown in Fig. 3.27, classical analogues of the strong ($\kappa > \Delta\omega_c, \Delta\omega_s$), weak ($\kappa < \Delta\omega_s, \Delta\omega_c$), and EIT ($\Delta\omega_s < \kappa < \Delta\omega_c$)

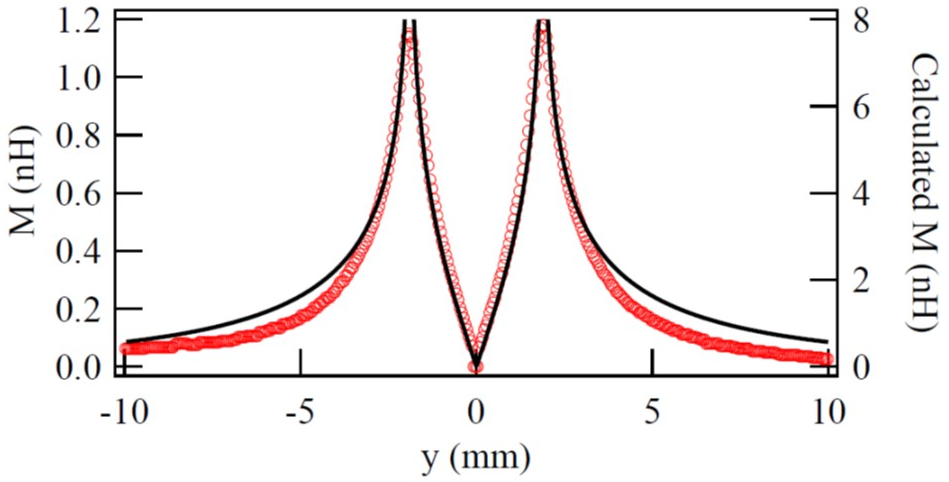

Figure 3.26: Experimentally obtained (symbol) and theoretically calculated (solid line) mutual inductance curve as a function of the separation y between the resonators.

coupling regimes can be achieved by using this pseudo CMP system. Furthermore by tuning the quality factor of the SRR by adding additional resistance, it should be possible to use this system to classically observe the Purcell ($\Delta\omega_c < \kappa < \Delta\omega_s$) coupling regime as well. Figure 3.28(a)-(d) show a plot of the typical transmission spectra as a function of the microwave frequency that correspond to the EIT, strong, weak, and Purcell coupling regimes, respectively simulated by using Eq. (3.19). The simulation parameters that were used have been listed in Table 3.1.

Range	$\kappa/2\pi$ (GHz)	$\Delta\omega_c$ (GHz)	$\Delta\omega_s$ (GHz)
EIT	0.05	0.3	0.001
Strong	0.45	0.15	0.05
Weak	0.05	0.15	0.06
Purcell	0.4	0.35	1

Table 3.1: Simulation parameters

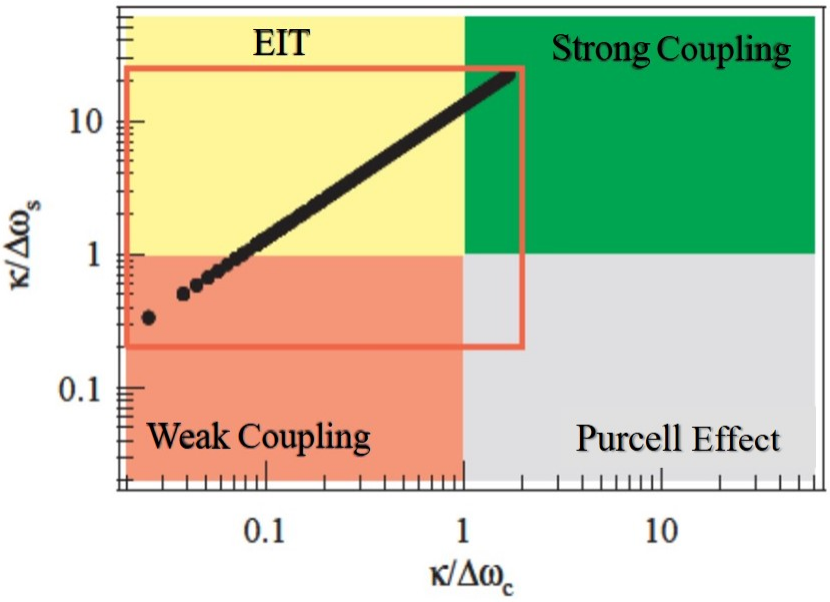

Figure 3.27: The different coupling regimes, as defined by Zhang et. al.[15], that were classically observed by changing the distance between the metamaterial resonators.

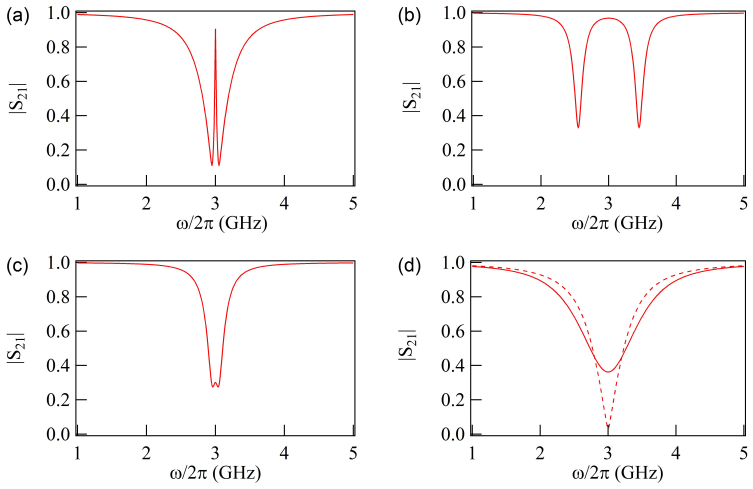

Figure 3.28: Simulated transmission curves corresponding to (a) EIT (b) strong (c) weak and (d) Purcell coupling regimes. The parameters used for these results have been listed in Table 3.1. The dashed curve in (d) shows the simulated transmission through the cut-wire alone.

3.4.3 Voltage Control of Metamaterial EIT

The high tunability of the artificial CMP device allows the fabrication of an on-chip microwave device that exhibits tunable EIT. Based on the dependence of mutual inductance/coupling strength between the cavity and pseudo magnon mode, an appropriate coupling regime ($\Delta\omega_s < \kappa < \Delta\omega_c$) was selected to demonstrate this active voltage control of the transparency window associated with EIT that is generated due to electrodynamic coupling. To do so, a varactor loaded SRR (similar to the one described in the previous section) with a Skyworks SMV 2019 varactor diode was fabricated at a distance of 4 mm from the cut wire as shown by the schematic diagram in Fig. 3.29. Here again, two r-f chokes were soldered on either side of the varactor diode to decouple the DC and microwave current circuits. The DC voltage was then applied across the edge of the SRR which contains the diode. The capacitance of the varactor diode can be changed from 2.2 pF to 0.3 pF[42] by applying a DC voltage which changes the resonance frequency of the SRR while the resonance frequency of the cut-wire remains the same.

Figure 3.30(a) shows some typical spectra obtained at different values of applied DC voltage. As shown in the figure, both resonances can be observed even when $\omega_s \neq \omega_c$ due to the mutual coupling between the pseudo cavity photon-magnon system. However, the amplitude of the resonance of the SRR is an order of magnitude weaker compared with that of the cut wire resonator when ω_s is far away from ω_c. This indicates less-efficient energy transfer from the cut-wire resonator to the

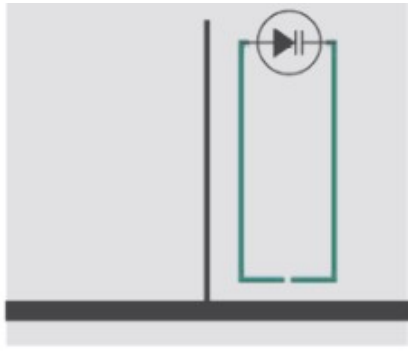

Figure 3.29: Schematic diagram of the fabricated varactor loaded SRR coupled with a cut-wire resonator located 4 mm away.

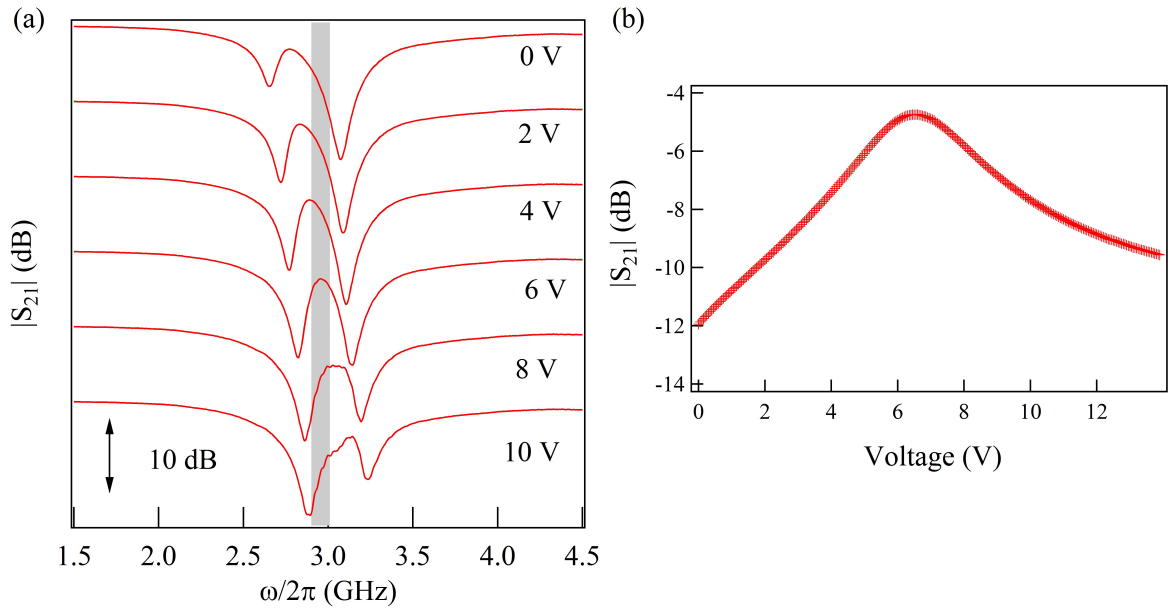

Figure 3.30: (Offset for clarity) (a) Typical transmission spectra plotted as a function of frequency at different values of applied voltage. (b) Microwave transmission at 3 GHz plotted as a function of the applied voltage.

SRR. The transmission at the resonance of the SRR is significantly enhanced when ω_s approaches ω_c. The two subsystems have identical resonance, i.e. $\omega_c/2\pi = \omega_s/2\pi$ = 3 GHz at the applied DC voltage of about 6.5 V. Here the bright mode (cut wire resonance) and the dark mode (SRR's resonance) both have equal amplitudes and the coupling between them leads to the generation of a Rabi gap of pseudo-CMP (of about 0.3 GHz) that creates a transparency window associated with EIT near 3 GHz. The microwave transmission measured at 3 GHz has been plotted as a function of the applied voltage in Fig. 3.30(b) where maximum transmission due to the generation of the Rabi gap of pseudo-CMP at around 6.5 V can be seen clearly. As shown in this figure, as the applied voltage increases, the device changes from being opaque to being transparent and then to being partially transparent at 3 GHz.

Figure 3.31(a) shows the experimentally measured dispersion of the artificial CMP in this voltage controlled device. This figure clearly shows the hybridization of the pseudo magnon and cavity modes which generates photon like and pseudo magnon-like polaritons separated by a gap near 3 GHz. The generation of EIT-like tranmission window in this system can be explained as follows.

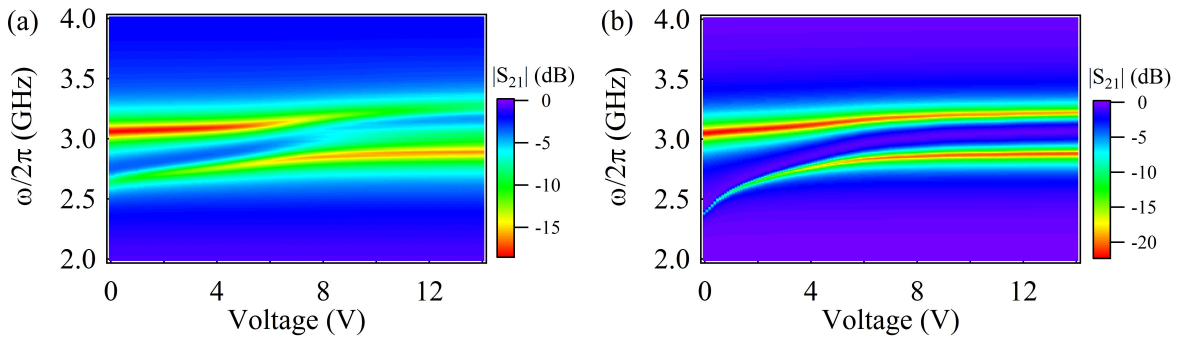

Figure 3.31: (a) Measured and (b) calculated transmission amplitude mapping obtained by continuously tuning the DC voltage applied to the varactor loaded SRR cavity.

In a coherent coupling system consisting of a cavity mode and a magnon mode, when the dissipation of the cavity mode becomes dominant, a transparency window in the transmission similar to the classical EIT can be observed when the resonance frequency of the two modes is matched. While the study in Ref. [15] has used the applied magnetic field to tune this transparency window by tuning the resonance frequency of the magnon mode, here the resonance frequency of the pseudo magnon-mode is tuned by tuning the applied voltage. This controls the efficiency of energy transfer between the cavity mode and the pseudo magnon mode. By tuning the voltage bias, the resonance frequency of the two modes is matched. Dominated by the dissipation of the cavity mode, there is efficient energy transfer between the two modes which creates EIT like profile in this system.

The dispersion of this device can also be calculated by using Eq. (3.19) by integrating the equivalent circuit for the varactor diode which includes multiple electronic elements. For simplicity, it is assumed that only the capacitance varies with the external applied DC voltage. Assuming C_v of the varactor is in series connection with $C_s = 2.7$ pF for a SRR with L_s = 0.88 nH, the transmission mapping is calculated as shown in Fig. 3.31(b) which qualitatively reproduces the observed EIT-like feature in the coupled pseudo CMP system.

The quantitative differences between Fig. 3.31(a) and (b) can be attributed to the effect of impedance mismatch between the 50Ω microstrip line and the 150Ω SRR line, or to the simplicity of the circuit used for the varactor diode and the saturation of the capacitance of the varactor

diode at higher voltages or to a combination of these two effects. Moreover, while varactor loaded microstrip resonators have been studied in the past[84, 85], here the varactor diode is used to tune the response of the SRR which in turn tunes the response of the entire device due to mutual electrodynamic coupling.

Therefore, by using the concept of artificial CMP, an on-chip hybrid device has been fabricated where the pseudo magnon-photon gap is produced due to electrodynamic coupling. This device can thus be used to achieve voltage tunable EIT in the microwave regime. The pseudo magnon-photon coupling can be well-explained by the transmission line model that has been developed. This system has the advantage of being easily tunable and therefore could be used for the classical observation of different coupling regimes. Moreover, since this system is planar and relies on voltage instead of magnetic control of the EIT transparency window, it could easily be adapted for potential practical applications in fabricating dynamic filters and to switch devices. This work has been published in the Journal of Physics D, Applied Physics[86].

Chapter 4

Summary

This thesis reports the results of three experimental studies that are based on the recently emerged but extensively investigated field of cavity photon-magnon coupling which leads to the generation of CMP. The focus of these experiments was to develop additional methods to control and study the cavity photon-magnon coupling. The results of these studies could also help in easier integration of the CMP system to on-chip devices for the various advanced spintronic applications that have been proposed[16, 17]. For the development of these applications, strong cavity photon-magnon coupling is required. This strong coupling can be achieved at room temperature by using a ferro/ ferrimagnetic sample that has a high spin density and low Gilbert damping as the coupling strength is proportional to the square root of the number of spins in the magnetic sample[15]. Therefore, for the purpose of cavity photon-magnon coupling experiments an YIG sample, that has a high spin density and low Gilbert damping, was used as a source of magnons.

The CMP system can be theoretically described by the classical harmonic oscillator or the quantum Hamiltonian or the classical electrodynamics model. Each of these three models and their relative advantages have been presented in detail in the Theory chapter of this thesis. At room temperature, for a bulk spin system, the quantum Hamiltonian model converges to the harmonic oscillator model in the rotating wave approximation. Thus, the quantum and the two classical models give a similar 2 x 2 matrix that can be used to model the cavity photon-magnon coupling

with the only difference being in the definition of the coupling parameter that describes the coupling strength between the cavity photon and the magnon in each model. The resonance frequency dispersion and the linewidth evolution of the cavity photon-magnon modes can then be modelled by using the real and imaginary parts of the eigen-frequencies of this matrix, respectively. The advantage of using this 2 x 2 matrix is that it can be easily extended to describe the coupling between multiple cavity photon and magnon modes. In this thesis, the 2 x 2 matrix obtained from the classical harmonic oscillator model was extended and modified to describe the various experimental results that were obtained.

In order to achieve the objective of making the cavity photon-magnon coupled system more suitable for potential practical applications, an artificially engineered structure known as a split ring resonator (SRR) has been used in this work. As described in Chapter 3, the SRR is made of a non-magnetic conducting material and is designed such that it has an effective magnetic permeability in the presence of microwave radiation due to which it can be used a source of pseudo-magnons. Furthermore, the SRR can be oriented in such a way that it is excited by both the electric and magnetic fields of the incident electromagnetic radiation. This induces a strong current in the SRR which allows it to either enhance/oppose the incident electromagnetic radiation due to which it also has the potential of being used as a cavity for cavity photon-magnon coupling experiments.

Therefore, a voltage tunable varactor loaded SRR that could be excited by using a tapered microstrip line was adapted to be used as a cavity for the first set of cavity photon-magnon experiments. By tuning the applied voltage, the capacitance of the varactor diode can be changed which in turn changes the resonance frequency of the varactor loaded SRR cavity. Experimentally, a spherical YIG sample was chosen as a source of magnons. The YIG sample characterization using a tapered microstrip line revealed that different long wavelength spin waves (known as magnetostatic modes) were excited due to the non-uniform microwave distribution across the YIG sphere. Furthermore, it was revealed that two of these magnetostatic modes were coupled to each other due to the effect of the dipole-dipole and exchange interactions on the dispersion of these modes. This coupling leads to the typical mode anti-crossing and linewidth exchange behaviour which can

be well-explained by the classical harmonic oscillator model.

The cavity photon-magnon coupling between the planar varactor loaded SRR cavity and the YIG sphere was then experimentally studied. The advantage of this varactor loaded cavity is that it not only allows the cavity photon-magnon coupling to be studied in the traditional way of tuning the applied magnetic field to tune the resonance frequency of the magnon modes but also allows to tune the resonance frequency of the cavity mode and hence tune the coupling between the photon-magnon modes. Hence, the cavity photon-magnon coupling was studied using both these methods and it was revealed that the two coupled magnetostatic modes interact differently with the cavity mode i.e. one of the magnetostatic modes was found to be strongly coupled with the cavity mode; whereas, the other magnetostatic mode was found to have no coupling with the cavity mode. This difference in their relative coupling strengths may be due to the difference in their respective mode magnetizations which could be further studied in the future. Nonetheless, the coupling between these two magnetostatic modes along with the cavity mode, examined using both the methods, can be well-described by extending the classical 2 x 2 matrix model to a 3 x 3 matrix model.

This voltage control of CMP using a planar varactor loaded SRR cavity would allow the design of an on-chip CMP system. This system would simply consist of a battery and a permanent magnet and hence would be more suitable for potential practical applications as it would eliminate the need of a big electromagnet that has been traditionally used to investigate the cavity photon-magnon coupling. However, for planar CMP systems, a quantitative simulation of the non-resonant radiation damping is essential which was also investigated in detail in this work.

The 2 x 2 matrix model that is used to describe the cavity photon-magnon coupling takes into account the resonant or the Gilbert damping of the magnon mode. This damping is responsible for the linewidth exchange between the cavity photon-magnon modes in CMP experiments. However, due to the precession of magnetic dipoles, the magnetic dipole radiation is produced which acts as a non-resonant radiation damping in CMP experiments. The effect of this non-resonant radiation damping was taken into account by adding an additional relaxation channel in the 2 x 2 matrix model. An LCR circuit model was also built based on this modified matrix model for

the purpose of quantitative simulations. The main predictions from this modified matrix model were that the effect of the non-resonant radiation damping becomes apparent only when the cavity photon-magnon resonance frequencies are far away from each other and that this additional damping causes the magnon resonance frequency to shift higher and the linewidth of the magnon mode to become broader. These predictions were verified experimentally by using a planar stripline cavity along with an YIG sphere. Here, it was found that this shift in the magnon resonance frequency and linewidth was proportional to the square of the coupling strength between the cavity photon-magnon modes. Hence, this experimental realization and theoretical modelling of the non-resonant radiation damping might help in the design and adaptation of planar CMP systems for potential practical applications.

To further remove the requirement of the static magnetic field, in the final section of the Experiment and Results chapter, pseudo CMP coupling is explored by utilizing the magnetic response of a SRR in order to replace the YIG sample as a source of magnons. Here, a planar cut-wire resonator was used as a cavity to excite the resonance of the SRR. In order to theoretically describe this planar coupled pseudo CMP system, a microwave transmission line model was built based on mutually coupled LCR circuits. The final result from this model was found to have a form that was similar to the CMP coupling model with the coupling strength being inversely proportional to the distance between the two resonators. Based on the ratio between the coupling strength and the linewidths of the two resonators, classical analogues of different coupling regimes can be defined such as the strong, weak, EIT and Purcell regimes. Using this definition of the different coupling regimes, a varactor loaded SRR was then used to show voltage control of metamaterial EIT. Here, the pseudo-CMP gap associated with the generation of pseudo-polaritons could be tuned by changing the applied voltage which tuned the transmission window associated with metamaterial EIT. This on-chip voltage control of metamaterial EIT could therefore be used in designing dynamic filters and to switch devices.

Hence, all the experimental works that have been discussed in this thesis were aimed at understanding the cavity photon-magnon coupling physics and developing systems that were better

suited for potential practical applications. Future work in this area could involve designing higher quality factor tunable circuit cavities in order to achieve effective control of cavity photon-magnon coupling. Furthermore, the ability to design and fabricate tunable cavities could be used to design a multi-terminal planar cavity wherein the effect of the input microwave phase at different input terminals could be used to achieve phase control of CMP. Moreover, the cavity photon-magnon coupling could be examined in the few photon, spin number limit at low temperatures. At this condition, it might be possible to observe and study the distinction between the classical and quantum coupling regimes.

Appendix A

Derivation of Classical Equations of Motion

As discussed in the first section of the Theory chapter of this thesis, the cavity photon-magnon coupling can be described by using a system of two coupled harmonic oscillators. In this chapter, the classical equations of motion that can be used to describe the cavity photon-magnon system will be derived starting from the Hamiltonian of the coupled system. This Hamiltonian would also be then compared with the quantum Hamiltonian that has been discussed previously [Eq. (2.4)].

The cavity photon-magnon system can be represented as a system of two harmonic oscillators with a unit mass and resonance frequency ω_c and ω_m, respectively. The kinetic energy of the oscillators when they are at a distance x_1, x_2 away from their equilibrium positions can therefore be written as

$$\begin{aligned} T_1 &= \frac{p_1^2}{2} = \frac{\dot{x}_1^2}{2}, \\ T_2 &= \frac{p_2^2}{2} = \frac{\dot{x}_2^2}{2}, \end{aligned} \tag{A.1}$$

where $\dot{x}_1, \dot{x}_2$ are the velocities of the two oscillators with momentum p_1 and p_2, respectively.

The potential energy of the coupled system can be represented by V which is assumed to be only a function of the position of the two oscillators. This potential energy satisfies the equilibrium condition $-\frac{\partial V}{\partial x}\Big|_{x=x_0} = 0$ i.e. when the system is in equilibrium there will be no restoring forces acting on it. In the case of small oscillations of the system near the equilibrium condition, the

potential energy can be expanded near the equilibrium point as

$$V(X_1, X_2) = V(x_{01}, x_{02}) + \sum_{i=1}^{2} \left.\frac{\partial V}{\partial x_i'}\right|_{x_i'=x_{0i}} x_i + \frac{1}{2}\sum_{i,j=1}^{2} \left.\frac{\partial^2 V}{\partial x_i' x_j'}\right|_{\substack{x_i'=x_{0i} \\ x_j'=x_{0j}}} x_i x_j, \tag{A.2}$$

where, $X_i = x_{0i} + x_i$, with x_{0i} being the equilibrium positions[87]. The potential energy at the equilibrium position can be chosen to be zero. Here, the potential energy terms that are linear in displacement vanish due to the equilibrium condition mentioned above so that the only the quadratic terms are left. The potential energy of this system can thus be written as

$$V(x_1, x_2) = \frac{\omega_c^2 x_1^2}{2} + \frac{\omega_m^2 x_2^2}{2} + \kappa\omega_c^2 x_1 x_2, \tag{A.3}$$

where it is assumed that $\omega_c^2 = \left.\frac{\partial^2 V}{\partial x_1'^2}\right|_{x_1'=x_{01}}$, $\omega_m^2 = \left.\frac{\partial^2 V}{\partial x_2'^2}\right|_{x_2'=x_{02}}$, and $\kappa\omega_c^2 = \frac{1}{2}\left.\frac{\partial^2 V}{\partial x_1' \partial x_2'}\right|_{\substack{x_1'=x_{01} \\ x_2'=x_{02}}} + \frac{1}{2}\left.\frac{\partial^2 V}{\partial x_2' \partial x_1'}\right|_{\substack{x_1'=x_{01} \\ x_2'=x_{02}}}$.

Therefore, the Hamiltonian of the coupled system is given by

$$H = T_1 + T_2 + V(x_1, x_2) = \frac{\dot{x}_1^2}{2} + \frac{\dot{x}_2^2}{2} + \frac{\omega_c^2 x_1^2}{2} + \frac{\omega_m^2 x_2^2}{2} + \kappa\omega_c^2 x_1 x_2. \tag{A.4}$$

From the above Hamiltonian, the Lagrangian of the system can be calculated as being

$$L = T_1 + T_2 - V = \frac{\dot{x}_1^2}{2} + \frac{\dot{x}_2^2}{2} - \frac{\omega_c^2 x_1^2}{2} - \frac{\omega_m^2 x_2^2}{2} - \kappa\omega_c^2 x_1 x_2. \tag{A.5}$$

The effect of damping on the cavity photon and magnon system can be included by introducing frictional forces in this harmonic oscillator model. If the frictional force is assumed to be proportional to the velocity of the oscillator, then the dissipation energy $U_f \propto \frac{\dot{x}^2}{2}$[87] such that the frictional force is given by $F_f = -\frac{\partial U_f}{\partial \dot{x}}$. Therefore, the damping force acting on the cavity photon

and magnon system can be represented as

$$\begin{aligned} F_{f1} &= -\beta\omega_c\dot{x}_1, \\ F_{f2} &= -\alpha\omega_c\dot{x}_2. \end{aligned} \tag{A.6}$$

Here, $\beta\omega_c, \alpha\omega_c$ are the constants of proportionality for the dissipation energies of the cavity photon and magnon systems.

The equations of motion for this coupled oscillator system can then be obtained from

$$\frac{d}{dt}(\frac{\partial L}{\partial \dot{x}_i}) - \frac{\partial L}{\partial x_i} = F_{fi} \tag{A.7}$$

as being

$$\begin{aligned} \ddot{x}_1 + \omega_c^2 x_1 + \kappa\omega_c^2 x_2 &= -\beta\omega_c\dot{x}_1, \\ \ddot{x}_2 + \omega_m^2 x_2 + \kappa\omega_c^2 x_1 &= -\alpha\omega_c\dot{x}_2. \end{aligned} \tag{A.8}$$

Here, it is assumed that the only external force acting on the system is the frictional force. If it is assumed that the oscillator representing the cavity mode is being driven by an external force f then the above equations can be re-written as

$$\begin{aligned} \ddot{x}_1 + \omega_c^2 x_1 + \kappa\omega_c^2 x_2 &= -\beta\omega_c\dot{x}_1 + f, \\ \ddot{x}_2 + \omega_m^2 x_2 + \kappa\omega_c^2 x_1 &= -\alpha\omega_c\dot{x}_2. \end{aligned} \tag{A.9}$$

If the displacement of the oscillators x_1, x_2 are assumed to have a form of $A_c e^{-i\omega t}$ and $A_m e^{-i\omega t}$, respectively where A_c and A_m are the maximum amplitudes of oscillation, then the above equations of motion can be written as

$$\begin{aligned} \omega^2 A_c - \omega_c^2 A_c - \kappa\omega_c^2 A_m + i\omega\beta\omega_c A_c &= -f, \\ \omega^2 A_c - \omega_m^2 A_m - \kappa\omega_c^2 A_m + i\omega\alpha\omega_c A_m &= 0. \end{aligned} \tag{A.10}$$

or in matrix format as

$$\begin{bmatrix} \omega^2 - \omega_c^2 + i\omega\omega_c\beta & -\kappa\omega_c^2 \\ -\kappa\omega_c^2 & \omega^2 - \omega_m^2 + i\omega\omega_c\alpha \end{bmatrix} \begin{bmatrix} A_c \\ A_m \end{bmatrix} = \begin{bmatrix} -f \\ 0 \end{bmatrix}. \tag{A.11}$$

The determinant of the 2 x 2 matrix given above is

$$det(\Omega) = (\omega^2 - \omega_c^2 + i\omega\omega_c\beta)(\omega^2 - \omega_m^2 + i\omega\omega_c\alpha) - \kappa^2\omega_c^4. \tag{A.12}$$

The real and imaginary parts of the roots of the above equation have been plotted as a function of the detuning $\Delta = \omega_m - \omega_c$ in Fig. A.1 (a) and (b), respectively which show the frequency dispersion and the linewidth evolution of the two hybridized modes produced due to coupling. The parameters used here for computation were $\omega_c = 2, \alpha = 0.0002, \beta = 0.03$ and $\kappa = 0.15$. For the case when $\alpha, \beta \ll 1$, Eq. (A.12) can be simplified as $det(\Omega) = (\omega^2 - \omega_c^2)(\omega^2 - \omega_m^2) - \kappa^2\omega_c^4 = 0$ from which the roots can be calculated near the coupling point $\omega \simeq \omega_c \simeq \omega_m$ to be

$$\omega_\pm = \frac{\omega_c + \omega_m \pm \sqrt{(\omega_c - \omega_m)^2 + \kappa^2\omega_c^2}}{2}. \tag{A.13}$$

From the above equation, it can be seen that the coupling between the two oscillators produces two hybridized modes, with resonance frequency ω_+ and ω_- such that $\omega_+ > \omega_-$. The eigenvectors ($[x_+, y_+]$ and $[x_-, y_-]$) corresponding to these two eigenfrequencies (ω_+ and ω_-, respectively) can be calculated for the case when $\alpha, \beta \ll 1$. If it is assumed that $\omega^2 - \omega_c^2 = 2\omega_c(\omega - \omega_c)$, and $\omega^2 - \omega_m^2 = 2\omega_c(\omega - \omega_m)$, the matrix equation for eigenvectors can be simplified as

$$\begin{bmatrix} 2(\omega_+ - \omega_c) & -\kappa\omega_c \\ -\kappa\omega_c & 2(\omega_+ - \omega_m) \end{bmatrix} \begin{bmatrix} x_+ \\ y_+ \end{bmatrix} = \begin{bmatrix} \Omega + \Delta & -\kappa\omega_c \\ -\kappa\omega_c & \Omega - \Delta \end{bmatrix} \begin{bmatrix} x_+ \\ y_+ \end{bmatrix} = 0, \tag{A.14}$$

where $\Delta = \omega_m - \omega_c, \Omega = \sqrt{(\omega_c - \omega_m)^2 + \kappa^2\omega_c^2}$. The normalized eigenvector is then given by

$$\begin{bmatrix} x_+ \\ y_+ \end{bmatrix} = \frac{1}{\sqrt{\kappa^2\omega_c^2 + (\Delta+\Omega)^2}} \begin{bmatrix} \kappa\omega_c \\ \Omega+\Delta \end{bmatrix}. \tag{A.15}$$

Assuming that $\sin\theta = \dfrac{\kappa\omega_c}{\Omega}$ and $\cos\theta = \dfrac{\Delta}{\Omega}$ then,

$$\begin{bmatrix} x_+ \\ y_+ \end{bmatrix} = \frac{1}{\sqrt{2\Omega^2(1+\cos\theta)}} \begin{bmatrix} \Omega\sin\theta \\ \Omega(1+\cos\theta) \end{bmatrix} = \frac{1}{2\cos(\theta/2)} \begin{bmatrix} \sin\theta \\ (1+\cos\theta) \end{bmatrix} \tag{A.16}$$

$$\begin{bmatrix} x_+ \\ y_+ \end{bmatrix} = \frac{1}{\sqrt{2}} \begin{bmatrix} \sqrt{1-\cos\theta} \\ \sqrt{1+\cos\theta} \end{bmatrix} = \frac{1}{\sqrt{2\Omega}} \begin{bmatrix} \sqrt{\Omega-\Delta} \\ \sqrt{\Omega+\Delta} \end{bmatrix}. \tag{A.17}$$

Similarly, the eigenvector corresponding to ω_- can be calculated and is given by

$$\begin{bmatrix} x_- \\ y_- \end{bmatrix} = \frac{1}{\sqrt{2}} \begin{bmatrix} -\sqrt{1+\cos\theta} \\ \sqrt{1-\cos\theta} \end{bmatrix} = \frac{1}{\sqrt{2\Omega}} \begin{bmatrix} -\sqrt{\Omega+\Delta} \\ \sqrt{\Omega-\Delta} \end{bmatrix}. \tag{A.18}$$

The eigenvectors corresponding to ω_+ and ω_- have been plotted as a function of the detuning (Δ) in Fig. A.1 (c) and (d), respectively with $\kappa = 0.15$ and $\omega_c = 2$.

A special case arises when $\omega_c = \omega_m$ i.e. the resonance frequency of the two oscillators is matched. In this case, Eq. (A.13) can be further simplified such that

$$\omega_\pm = \omega_c \pm \frac{\kappa\omega_c}{2}. \tag{A.19}$$

Then, $\Omega = \sqrt{\Delta^2 + \kappa^2\omega_c^2} = \kappa\omega_c$ and the two eigenvectors calculated above can be simplified as being

$$\begin{bmatrix} x_+ \\ y_+ \end{bmatrix} = \frac{1}{\sqrt{2\Omega}} \begin{bmatrix} \sqrt{\Omega-\Delta} \\ \sqrt{\Omega+\Delta} \end{bmatrix} = \frac{1}{\sqrt{2}} \begin{bmatrix} 1 \\ 1 \end{bmatrix}, \tag{A.20}$$

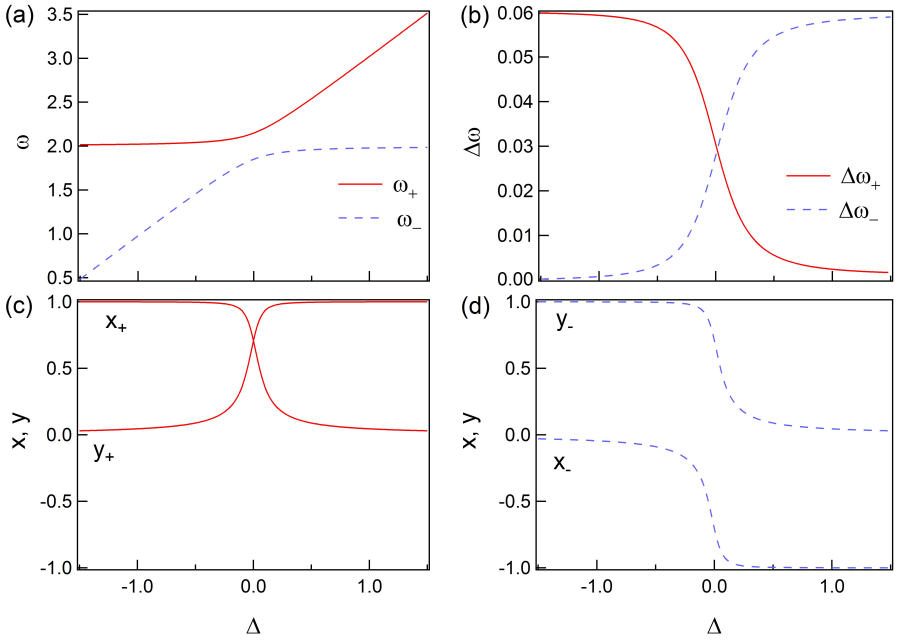

Figure A.1: The (a) eigenfrequency, (b) linewidth, (c) and (d) eigenvectors for the two hybridized modes plotted as a function of the detuning Δ.

$$\begin{bmatrix} x_- \\ y_- \end{bmatrix} = \frac{1}{\sqrt{2\Omega}} \begin{bmatrix} -\sqrt{\Omega+\Delta} \\ \sqrt{\Omega-\Delta} \end{bmatrix} = \frac{1}{\sqrt{2}} \begin{bmatrix} -1 \\ 1 \end{bmatrix}. \tag{A.21}$$

The above equations show that the coupling between the two oscillators produces two hybridized modes in which the oscillators are either moving in the same direction with a resonance frequency of ω_+ or they are moving in the opposite direction with a resonance frequency of ω_-. The motion of the oscillators for these two cases has been shown in Fig. A.2 (a) and (b), respectively.

For the coupled cavity photon-magnon system described above in terms of the classical harmonic oscillator model, the interaction term in the potential V given by Eq. (A.3) was positive i.e. $\frac{1}{2}\frac{\partial^2 V}{\partial x_1' \partial x_2'}\Big|_{\substack{x_1'=x_{01} \\ x_2'=x_{02}}} + \frac{1}{2}\frac{\partial^2 V}{\partial x_2' \partial x_1'}\Big|_{\substack{x_1'=x_{01} \\ x_2'=x_{02}}} = \kappa\omega_c^2 > 0$. However, this classical harmonic oscillator model is general and can be applied to other coupled systems in which the interaction term of the potential can also be negative. For example, consider the atomic system, where two atoms combine to form a molecule by forming bonding and anti-bonding molecular orbitals. The bonding orbitals are lower in energy than the orbitals of the separate atoms and correspond to in-phase interactions

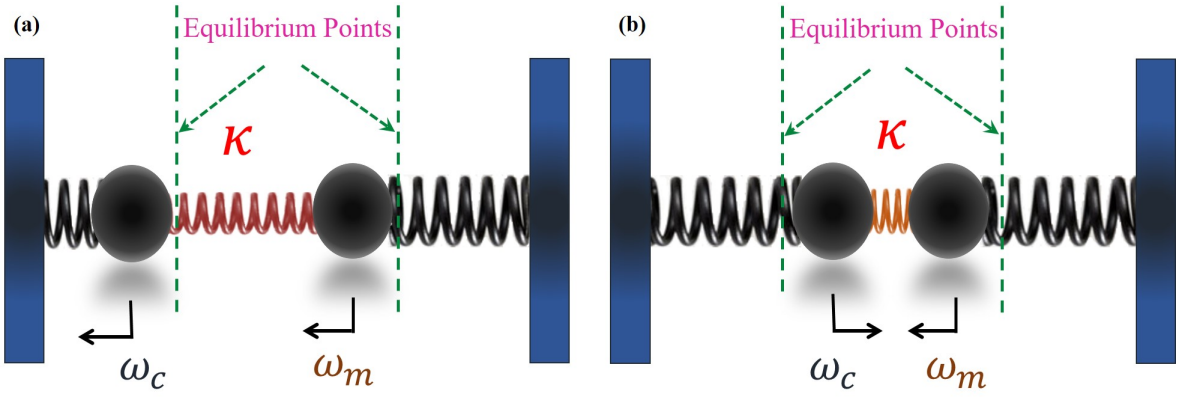

Figure A.2: The two hybridized oscillation modes generated due to coupling in which the oscillators oscillate (a) in the same direction with a resonance frequency ω_+ and (b) in the opposite direction with a resonance frequency ω_-.

between the atomic orbitals, whereas the anti-bonding molecular orbitals are higher in energy than the orbitals of the separate atoms and correspond to out of phase interactions between the atomic orbitals. This difference in the energy levels of the in phase and out of phase eigenstates for the molecular orbital case compared to the cavity photon-magnon coupled case (wherein the in phase oscillation had a higher energy than the out of phase oscillation) can be explained as follows. When two atoms combine to form a molecule, their binding energy is negative which corresponds to the case that the interaction term in the potential V given by Eq. (A.3) is negative. In this case, the potential energy V can be modelled as being the potential energy due to a spring that is connected to two oscillating masses such that $V = \frac{\kappa\omega_c^2(x_2 - x_1)^2}{2}$[87]. Then, the modified equations of motion in matrix format (in the absence of damping) are

$$\begin{bmatrix} \omega^2 - \omega_c^2 & \kappa\omega_c^2 \\ \kappa\omega_c^2 & \omega^2 - \omega_m^2 \end{bmatrix} \begin{bmatrix} A_c \\ A_m \end{bmatrix} = \begin{bmatrix} -f \\ 0 \end{bmatrix}. \tag{A.22}$$

The eigenvalues of this system are equal to the eigenvalues of the coupled cavity photon-magnon system given by Eq. (A.13) (with $\beta, \alpha = 0$) but the eigenvectors for ω_+ and ω_-, when $\omega_c = \omega_m$ are now given by

$$\begin{bmatrix} x_+ \\ y_+ \end{bmatrix} = \frac{1}{\sqrt{2}} \begin{bmatrix} -1 \\ 1 \end{bmatrix}, \tag{A.23}$$

$$\begin{bmatrix} x_- \\ y_- \end{bmatrix} = \frac{1}{\sqrt{2}} \begin{bmatrix} 1 \\ 1 \end{bmatrix}, \tag{A.24}$$

respectively. Therefore, the above equations clearly show that when the interaction term of the potential energy is negative (which corresponds to a negative binding energy), the out of phase interaction has a higher eigenfrequency and hence a higher energy than the in-phase interaction. Thus, the sign of the interaction term of the potential energy governs the energy of the hybridised eigenstates of the system and is dependent on whether the binding energy is positive (as is the case for cavity photon-magnon systems) or negative (for molecular orbital systems).

The Hamiltonian derived above using classical mechanics [Eq. (A.4)] can also be compared with the Hamiltonian that was obtained by using microscopic quantum theory [Eq. (2.4)] discussed in Section 2.2. This quantum Hamiltonian is given by

$$H/\hbar - \frac{\omega_c + \omega_m}{2} = \omega_m m^\dagger m + \omega_c p^\dagger p + \kappa_q (p^\dagger m + m^\dagger p). \tag{A.25}$$

Here, $p^\dagger = \sqrt{\frac{\omega_c}{2\hbar}}(x_p - \frac{ip_p}{\omega_c})$, $p = \sqrt{\frac{\omega_c}{2\hbar}}(x_p + \frac{ip_p}{\omega_c})$, $m^\dagger = \sqrt{\frac{\omega_m}{2\hbar}}(x_m - \frac{ip_m}{\omega_c})$, and $m = \sqrt{\frac{\omega_m}{2\hbar}}(x_m + \frac{ip_m}{\omega_m})$ are the photon and magnon creation and annihilation operators, respectively expressed in terms of the position x_p, x_m and momentum p_p, p_m operators used in the context of quantum harmonic oscillators with a unit mass. Therefore, by using this definition of the creation and annihilation operators, the above equation can be written as

$$\frac{H}{\hbar} - \frac{\omega_c + \omega_m}{2} = \frac{\omega_c^2}{2\hbar}(x_p^2 - \frac{\hbar}{\omega_c} + \frac{p_p^2}{\omega_c^2}) + \frac{\omega_m^2}{2\hbar}(x_m^2 - \frac{\hbar}{\omega_m} + \frac{p_m^2}{\omega_m^2}) + \kappa_q \frac{\sqrt{\omega_c \omega_m}}{2\hbar}(2x_p x_m + \frac{2p_p p_m}{\omega_c \omega_m}), \tag{A.26}$$

or simplified as being

$$H = \frac{\omega_c^2 x_p^2}{2} + \frac{p_p^2}{2} + \frac{\omega_m^2 x_m^2}{2} + \frac{p_m^2}{2} + \kappa_q \sqrt{\omega_c \omega_m} x_p x_m + \kappa_q \frac{p_p p_m}{\sqrt{\omega_c \omega_m}}. \tag{A.27}$$

In the above equation, if the momentum coupled term is ignored then the Hamiltonian has the exact same form as the one obtained from classical mechanics [Eq. (A.4)] with the only difference being in the definition of the coupling constant κ and κ_q. Therefore, the classical and quantum Hamiltonians that can be used to describe the coupled cavity photon-magnon system in terms of harmonic oscillators are equivalent. Hence, either of these two models can be used to study the cavity photon-magnon system.

Appendix B

List of Publications

S. Kaur, B. M. Yao, J. W. Rao, Y. S. Gui, and C.-M. Hu. Voltage control of cavity magnon polariton. *Appl. Phys. Lett.* **109**, 032404, (2016).

S. Kaur, B. M. Yao, Y. S. Gui, and C.-M. Hu. On-chip artificial magnon-polariton device for voltage control of electromagnetically induced transparency. *J. Phys. D: Appl. Phys.* **49**, 475103 (2016).

J. W. Rao, **S. Kaur**, X. L. Fan, D. S. Xue, B. M. Yao, Y. S. Guim and C.-M. Hu. Characterization of the non-resonant radiation damping in coupled cavity photon magnon system. *Appl. Phys. Lett.* **110**, 262404, (2017).

Bibliography

[1] D. Sanvitto, and S. K-Cohen. The road towards polaritonic devices. *Nat. Mat.* **15**, 1061, (2016).

[2] J. J. Hopfield. Theory of the contribution of excitons to the complex dielectric constant of crystals. *Phys. Rev.* **112**, 1555 (1958).

[3] D. L. Mills, and E. Burnstein. Polaritons: The electromagnetic modes of media. *Rep. Prog. Phys.*, **37**, 817, (1974).

[4] K. B. Tolpygo. Physical properties of a rock salt lattice made up of deformable ions. *Ukranian J. Phys.* **53**, 93 (2008).

[5] K. Huang. Lattice vibrations and optical waves in ionic crystals. *Nature* **167**, 779 (1951).

[6] R. G. Ulbrich and C. Weisbuch. Resonant Brillouin scattering of excitonic polaritons in Gallium Arsenide. *Phys. Rev. Lett.* **38**, 865 (1977).

[7] H. Deng, H. Haug, and Y. Yamamoto. Exciton-polariton Bose-Einstein condensation. *Rev. Mod. Phys.* **82**, 1489, (2010).

[8] J. D. Plumhof, T. Stoferle, L. Mai, U. Scherf, and R. F. Mahrt. Room-temperature Bose–Einstein condensation of cavity exciton–polaritons in a polymer. *Nat. Mater.* **13**, 247, (2014).

[9] C. Weisbuch, M. Nishioka, A. Ishikawa, and Y. Arakawa. Observation of the coupled exciton-photon mode splitting in a semiconductor quantum microcavity. *Phys. Rev. Lett.* **69**, 3314, (1992).

[10] L. Bai, M. Harder, Y. P. Chen, X. Fan, J. Q. Xiao, and C.-M. Hu. Spin pumping in electrodynamically coupled magnon-photon systems. *Phys. Rev. Lett.* **114**, 227201, (2015).

[11] O. O. Soykal, and M. E. Flatte. Strong field interactions between a nanomagnet and a photonic cavity. *Phys. Rev. Lett.* **104**, 077202, (2010).

[12] C.-M. Hu. Dawn of Cavity Spintronics. *Phys. in Canada* **72** No. 2, 76, (2016).

[13] H. Huebl, C. W. Zollitsch, J. Lotze, F. Hocke, M. Greifenstein, A. Marx, R. Gross, and S. T. B. Goennenwein. High cooperativity in coupled microwave resonator ferrimagnetic insulator hybrids. *Phys. Rev. Lett.* **111**, 127003 (2013).

[14] Y. Tabuchi, S. Ishino, T. Ishikawa, R. Yamazaki, K. Usami, and Y. Nakamura. Hybridizing ferromagnetic magnons and microwave photons in the quantum limit. *Phys. Rev. Lett.* **113**, 083603, (2014).

[15] X. Zhang, C. -L. Zou, L. Jiang, and H. X. Tang. Strongly coupled magnons and cavity microwave photons. *Phys. Rev. Lett.* **113**, 156401, (2014).

[16] X. F. Zhang, C. L. Zou, N. Zhu, F. Marquardt, L. Jiang, H. X. Tang. Magnon dark modes and gradient memory. *Nat. Commun.* **6**, 8914 (2015).

[17] Y. Tabuchi, S. Ishino, A. Noguchi, T. Ishikawa, R. Yamazaki, K. Usami, and Y. Nakamura. Coherent coupling between a ferromagnetic magnon and a superconducting qubit. *Science* **349**, 405 (2015).

[18] M. Harder, L. Bai, C. Match, J. Sirker, and C.-M Hu. Study of the cavity-magnon-polariton transmission line shape. *Sci. China Phys. Mech. Astron.* **59**, 117511, (2016).

[19] P. Hyde, L. Bai, M. Harder, C. Dyck, and C.-M Hu. Linking magnon-cavity strong coupling to magnon-polaritons through effective permeability. *Phys. Rev. B.* **95**, 094416, (2017).

[20] N. J. Lambert, J. A. Haigh, and A. J. Ferguson. Identification of spin wave modes in yttrium iron garnet strongly coupled to a co-axial cavity. *J. Appl. Phys.* **117**, 053910, (2015).

[21] J. B. Pendry, A. J. Holden, D. J. Robbins, and W. J. Stewart. Magnetism from conductors and enhanced nonlinear phenomena. *IEEE Trans. Microwave Theory Tech.* **47**, 2075, (1999).

[22] D. R. Smith, W. J. Padilla, D. C. Vier, S.C. Nemat-Nasser, and S. Schultz. Composite medium with simultaneously negative permeability and permittivity. *Phys. Rev. Lett.* **84**, 4184, (2000).

[23] D. M. Pozar, *Microwave Engineering* 3rd Ed. (Wiley, New York, 2005).

[24] G. Antonini. A general framework for the analysis of metamaterial transmission lines. *Prog. in Electromag. Res. B.* **20**, 353, (2010).

[25] G. V. Eleftheriades , A. K. Iyer, P. C. Kremer. Planar negative refractive index media using periodically L-C loaded transmission lines. *IEEE Trans. Microw. Theory and Tech.* **50**, 2702, (2002).

[26] L. D. Landau and E. M. Lifshitz. Theory of the dispersion of magnetic permeability in ferromagnetic bodies. *Phys. Z. Sowietunion* **8**, 153, (1935).

[27] T. L. Gilbert. A Lagrangian formulation of the gyromagnetic equation of the magnetic field. *Phys. Rev.* **100**, 1243, (1955).

[28] N. Mecking, Y. S. Gui, and C.-M. Hu. Microwave photovoltage and photoresistance effects in ferromagnetic microstrips. *Phys. Rev. B* **76**, 224430, (2007).

[29] X. Wang, *Metallic Spintronic Devices*, CRC Press (2014).

[30] P. S. Carter. Design of magnetically tunable microwave filters using single crystal yttrium-iron-garnet resonators. *IRE. Trans. Microw. Theory and Tech.* **9**, 252, (1961).

[31] X. F. Zhang, C. -L. Zou, L. Jiang, H. X. Tang. Superstrong coupling of thin film magnetostatic waves with microwave cavity. *J. Appl. Phys.* **119**, 023905, (2016).

[32] Y. Cao, P. Yan, H. Huebl, S. T. B. Goennenwein, and G. E. W. Bauer. Exchange magnon polaritons in microwave cavities. *Phys. Rev. B* **91**, 094423, (2015).

[33] Adapted from Left-handed metamaterial array configuration (c) Cynthia. L. Dreibelbis, retrieved from $https : //commons.wikimedia.org/wiki/File :$ `Left-handed_metamaterialarray_configuration.jpg`.

[34] R. A. Shelby, D. R. Smith, S. C. Nemat-Nasser, and S. Schultz. Microwave transmission through a two-dimensional, isotropic, left-handed metamaterial. *Appl. Phys. Lett.* **78**, 489, (2001).

[35] V. G. Veselago. The electrodynamics of substances with simultaneously negative values of ϵ and μ. *Sov. Phys. Upsekhi*, **10**, 509, (1968).

[36] J. B. Pendry, D. Schurig and D. R. Smith. Controlling Electromagnetic Fields. *Science* **312**, 1780, (2006).

[37] H. J. Lee, and J. G. Yook. Biosensing using split-ring resonators at microwave regime. *Appl Phys. Lett.* **98**, 254103, (2008).

[38] A. A. Abduljabar, D. J. Rowe, A. Porch, and D. A. Barrow. Novel microwave microfluidic sensor using a microstrip split-ring resonator. *IEEE Trans. Microwave Theory Tech.* **62**, 679 (2014).

[39] B. Bhoi, T. Cliff, I. S. Maksymov, M. Kostylev, R. Aiyar, N. Venkataramani, S. Prasad, and R. L. Stamps. Study of photon–magnon coupling in a YIG-film split-ring resonant system. *J. Appl. Phys.* **116**, 243906, (2014).

[40] W. R. Xu and S. Sonkusale. Microwave diode switchable metamaterial reflector/absorber. *Appl. Phys. Lett.* **103**, 031902, (2013)

[41] N. Xiang, Q. Cheng, J. Zhao, T.J. Cui, H. F. Ma, and W. X. Jiang. Switchable zero-index metamaterials by loading positive-intrinsic-negative diodes. *Appl. Phys. Lett.* **104**, 053504, (2014)

[42] Skyworks Solution Inc (2014). Data Sheet SMV2019 to SMV2023 Series: Hyperabrupt Junction Tuning Varactors, Boston, U.S.A.

[43] B. Lax and K. J. Button, *Microwave Ferrites and Ferrimagnetics*, Mc Graw Hill, 1962.

[44] L. R. Walker. Magnetostatic modes in ferromagnetic resonance. *Phys. Rev. Lett.* **105**, 390, (1957).

[45] B. A. Kalinikos, and A. N. Slavin. Theory of dipole exchange spin wave spectrum for ferromagnetic films with mixed exchange boundary conditions. *J. Phys. C: Solid State Phys.* **19**, 7013, (1986).

[46] S. Kalarickal, P. Krivosik, M. Wu, C. E. Patton, M. L. Schneider, P. Kabos, T. J. Silva, J. Nibarger. Ferromagnetic resonance linewidth in metallic thin films: Comparison of measurement methods. *J. Appl. Phys.* **99**, 093909 (2006).

[47] G. Srinivasan and A. N. Slavin, *High Frequency Processes in Magnetic Materials*, World Scientific, 1995.

[48] D. N. Bose, S. R. Borgaonkar, and T. S. Vedavathy. Measurement of magnetic properties of single crystal YIG by non-resonant method. *Bull. Mater Sci.* **2**, 121, (1979).

[49] P. Roschmann, and H. Dotsch. Properties of magnetostatic modes in ferrimagnetic spheroids. *Phys. Stat. Sol.* **82**, 11, (1977).

[50] S. Kaur, B. M. Yao, J. W. Rao, Y. S. Gui, and C.-M. Hu. Voltage control of cavity magnon polariton. *Appl. Phys. Lett.* **109**, 032404, (2016).

[51] P. M. V. B. Barone, and A. O. Caldeira. Quantum mechanics of radiation damping. *Phys. Rev. A.* **43**, 57,(1991).

[52] M. P. Norton, and D. G. Karczub, [Chapter 3] *Fundamentals of Noise and Vibration Analysis for Engineers* 2nd Ed. (Cambridge University Press, Cambridge, 2003).

[53] C. Ropers, D. J. Park, G. Stibenz, G. Steinmeyer, J. Kim, D. S. Kim, and C. Lienau. Femtosecond light transmission and subradiant damping in plasmonic crystals. *Phys. Rev. Lett.* **94**, 113901, (2005).

[54] N. Bloembergen and R. V. Pound. Radiation damping in magnetic resonance experiments. *Phys. Rev.* **95**, 8 (1954).

[55] R. W. Sanders, D. Paquette, V. Jaccarino, and S. M, Rezende. Radiation damping in magnetic resonance. II. Continuous-wave antiferromagnetic-resonance experiments. *Phys. Rev. B.* **10**, 132, (1974).

[56] S. Chaudhuri, and F. Keffer. Classical and quantum theories of radiation damping in ferromagnetic and antiferromagnetic resonance. *J. Phys. Chem. Sol.* **45**, 47, (1984).

[57] G. Wende. Radiation damping in FMR measurements in a nonresonant rectangular waveguide. *Phys. Stat. Sol.* **36**, 557, (1976).

[58] M. A. W. Schoen, J. M. Shaw, H. T. Nembach, M. Weiler and T. J. Silva. Radiative damping in waveguide-based ferromagnetic resonance measured via analysis of perpendicular standing spin waves in sputtered permalloy films. *Phys. Rev. B.* **92**, 184417, (2015).

[59] H. Le Gall, B. Desormier, and E. Milot. Transient processes in spin-wave systems with magnetic dipole radiation—I. Theory. *J. Phys. Chem. Sol.* **30**, 979, (1969).

[60] A. B. Pippard, [Chapter 16] *The physics of vibration* (Cambridge University Press, Cambridge, 1969).

[61] J. W. Rao, S. Kaur, X. L. Fan, D. S. Xue, B. M. Yao, Y. S. Guim and C.-M. Hu. Characterization of the non-resonant radiation damping in coupled cavity photon magnon system. *Appl. Phys. Lett.* **110**, 262404, (2017).

[62] N. Papasimakis, and N. I. Zheludev. Metamaterial induced transparency sharp fano resonances and slow light. *Opt. and Photonics News.* **20**, 22, (2009).

[63] L. V. Hau, S. E. Harris, Z. Dutton, and C. H. Behroozi. Light speed reduction to 17 metres per second in an ultracold atomic gas. *Nature*, **397**, 594, (1999).

[64] S. E. Harris, J. E. Field, and A. Imamoglu. Non linear optical processes using electromagnetically induced transparency. *Phys. Rev. Lett.* **64**, 1107, (1990).

[65] M. I. Stockman, S. V. Faleev, and D. J. Bergman. Localization vs Delocalization of surface plasmons in nanosystems: Can one state have both characteristics? *Phys. Rev. Lett.* **87**, 167401, (2001).

[66] S. Zhang, D. A. Genov, Y. Wang, M. Liu, and X. Zhang. Plasmon induced transparency in metamaterials. *Phys. Rev. Lett.* **101**, 047401, (2008).

[67] V. A. Fedotov, M. Rose, S. L. Prosvernin, N. Papasimakis, N. I. Zheludev. Sharp trapped-mode resonances in planar metamaterials with broken structural symmetry. *Phys. Rev. Lett.* **99**, 147401, (2007).

[68] L. Zhu, L. Dong, F. Meng, J. Fu, Q. Wu. Influence of symmetry breaking in a planar metamaterial on transparency effect and sensing application. *Appl. Opt.* **51**, 7794, (2012).

[69] N. Liu, S. Kaiser, and H. Giessen. Magnetoinductive and electroinductive coupling in plasmonic metamaterial molecules. *Adv. Mat.* **20**, 4521, (2008).

[70] H. M. Li, S. B. Liu, S. Liu and S. F. Zhang. Electromagnetically induced transparency with large group index induced by simultaneously exciting the electric and magnetic resonance. *Appl. Phys. Lett.* **105**, 133514, (2014).

[71] F. Y. Meng, Q. Wu, D. Erni, K. Wu, J. C. Lee. Polarization independent metamaterial analog of electromagnetically induced transparency for a refractive index based sensor. *IEEE Trans. Microw. Theory and Tech.* **60**, 3013, (2012).

[72] P. Tassin, L. Zhang, R. Zhao, A. Jain, Th. Koschny and C. M. Soukoulis. Electromagnetically induced transparency and absorption in metamaterials: The radiating two-oscillator model and its experimental confirmation. *Phys. Rev. Lett.* **109**, 187401, (2012).

[73] J. Wallauer, and M. Walther. Fano-line shape and phase reversal in a split-ring resonator based metamaterial. *Phys Rev. B*, **88**, 195118, (2013).

[74] Z. G. Dong, P. G. Ni, J. Zhu, and X. Zhang. Transparency window for the absorptive dipole resonance in a symmetry-reduced grating structure. *Opt. Exp.* **20** 7206, (2012).

[75] Z. G. Dong, H. Liu, M. X. Xu, T. Li, S. M. Wang, J. X. Cao, S. N. Zhu, and X. Zhang. Role of asymmetric environment on the dark mode excitation in metamaterial analogue of electromagnetically-induced transparency. *Opt. Exp.* **18** 22412, (2010).

[76] N. Papasimakis, V. A. Fedotov, N. I. Zheludev, and S. L. Prosvirnin. Metamaterial analog of electromagnetically induced transparency. *Phys. Rev. Lett.* **101**, 253903 (2008).

[77] P. Tassin, L. Zhang, Th. Koschny, E. N. Economou and C. M Soukoulis. Low loss metamaterials based on classical electromagnetically induced transparency. *Phys. Rev. Lett.* **102**, 053901, (2009).

[78] N. Liu, T. Weiss, M. Mesch, L. Langguth, U. Eigenthaler, M. Hirscher, C. Sonnichsen, and H. Giessen. Planar metamaterial analogue of electromagnetically induced transparency for plasmonic sensing. *Nano Lett.* **10**, 1103, (2009).

[79] H. Tao, A. C. Strikwerda, K. Fan, W. J. Padilla, X. Zhang and R. D. Averitt. Reconfigurable terahertz metamaterials. *Phys. Rev. Lett*, **103**, 147401, (2009).

[80] J. Gu, R. Singh, X. Liu, X. Zhang, Y. Ma, S. Zhang, S. A. Maier, Z. Tian, A. K. Azad, H.T. Chen, A. J. Taylor, J. Han and W. Zhang. Active control of electromagnetically induced transparency analogue in terahertz metamaterials. *Nat. Comm.* **3**, 1151, (2012).

[81] J. Wu, B. Jin, J. Wan, L. Liang, Y. Zhang, T. Jia, C. Cao, L. Kang, W. Xu, J. Chen, and P. Wu. Superconducting terahertz metamaterials mimicking electromagnetically induced transparency. *Appl. Phys. Lett.* **99**, 161113, (2011).

[82] B. B. Jin, J. B. Wu, C. H. Zhang, X. Q. Jia, L. Kang, J. Chen, and P. H. Wu. Enhanced slow light in superconducting electromagnetically induced transparency metamaterials. *Supercond. Sci. Tech.* **26**, 074004, (2013).

[83] L. Fu, S. Schweizer, H. Guo, N. Liu, and H. Giessen. Analysis of metamaterials using transmission line models. *Appl. Phys. B,* **86**, 325, (2007).

[84] Z. P. Wang, P. S. Hall, J. Kelly, and P. Gardner. Microstrip tunable bandpass filter with the colinear resonators. *Int. J. Antennas Propag.* **2013**, 960138, (2013).

[85] B. Kapilevich, and R. Lukjanets. Optimization of varactor tunable microstrip resonators for wireless applications. *MIA-ME'99 Proc. IEEE -Russia Conf.* II60-II67, (1999).

[86] S. Kaur, B. M. Yao, Y. S. Gui, and C.-M. Hu. On-chip artificial magnon-polariton device for voltage control of electromagnetically induced transparency. *J. Phys. D: Appl. Phys.* **49**, 475103 (2016).

[87] H. Goldstein, C. Poole, and J. Safko, *Classical Mechanics*, 3rd ed. (Addison Wesley, San Francisco, 2001).